Publications of the Astronomical Society of Japan, 2025, **77**(SP1), S171–S187
https://doi.org/10.1093/pasj/psaf091
Advance access publication date: 2025 September 11

XRISM observations of Cassiopeia A: Overview, atomic data, and spectral models

Paul Plucinsky,[1,*] Manan Agarwal,[2,*] Liyi Gu,[3] Adam Foster,[1] Toshiki Sato,[4] Aya Bamba,[5,6,7] Jacco Vink,[2,3] Masahiro Ichihashi,[5] Kai Matsunaga,[8] Koji Mori,[9] Hiroshi Nakajima,[10] Frederick S. Porter,[11] Haruto Sonoda,[5,12] Shunsuke Suzuki,[12,13] Dai Tateishi,[5] Yukikatsu Terada,[14,12] Hiroyuki Uchida,[8] and Hiroya Yamaguchi[12]

[1]Center for Astrophysics, Harvard-Smithsonian, 60 Garden St, Cambridge, MA 02138, USA
[2]Anton Pannekoek Institute/GRAPPA, University of Amsterdam, Science Park 904, 1098 XH Amsterdam, The Netherlands
[3]SRON Netherlands Institute for Space Research, Niels Bohrweg 4, 2333 CA Leiden, The Netherlands
[4]School of Science and Technology, Meiji University, 1-1-1 Higashi-Mita, Tama-ku, Kawasaki, Kanagawa 214-8571, Japan
[5]Department of Physics, Graduate School of Science, The University of Tokyo, 7-3-1 Hongo, Bunkyo-ku, Tokyo 113-0033, Japan
[6]Research Center for the Early Universe, School of Science, The University of Tokyo, 7-3-1 Hongo, Bunkyo-ku, Tokyo 113-0033, Japan
[7]Trans-Scale Quantum Science Institute, The University of Tokyo, 7-3-1 Hongo, Bunkyo-ku, Tokyo 113-0033, Japan
[8]Department of Physics, Kyoto University, Kitashirakawa Oiwakecho, Sakyo-ku, Kyoto, Kyoto 606-8502, Japan
[9]Faculty of Engineering, University of Miyazaki, 1-1 Gakuen-kibanadai-nishi, Miyazaki, Miyazaki 889-2192, Japan
[10]College of Science and Engineering, Kanto Gakuin University, 1-50-1 Mutsuura-higashi, Kanazawa-ku, Yokohama, Kanagawa 236-8501, Japan
[11]NASA Goddard Space Flight Center, Greenbelt, MD 20771, USA
[12]ISAS/JAXA, 3-1-1 Yoshinodai, Chuo-ku, Sagamihara, Kanagawa 252-5210, Japan
[13]Department of Science and Engineering, Graduate School of Science and Engineering, Aoyama Gakuin University, 5-10-1 Fuchinobe, Sagamihara, Kanagawa 252-5258, Japan
[14]Graduate School of Science and Engineering, Saitama University, 255 Shimo-Ohkubo, Sakura, Saitama, Saitama 338-8570, Japan
*E-mail: pplucinsky@cfa.harvard.edu; m.agarwal@uva.nl

Abstract

Cassiopeia A (Cas A) is the youngest known core-collapse supernova remnant in the Galaxy and is perhaps the best-studied supernova remnant in X-rays. Cas A has a line-rich spectrum dominated by thermal emission and, given its high flux, it is an appealing target for high-resolution X-ray spectroscopy. Cas A was observed at two different locations during the Performance Verification phase of the X-ray Imaging and Spectroscopy Mission (XRISM), one location in the south-eastern part of the remnant and one in the north-western part. This paper serves as an overview of these observations and in it we discuss some of the issues relevant for the analysis of the data. We present maps of the so-called spatial-spectral mixing effect due to the fact that the XRISM point-spread function is larger than a pixel in the Resolve calorimeter array. We analyze spectra from two bright, on-axis regions such that the effects of spatial-spectral mixing are minimized. We fit these spectra with a semi-empirical model consisting of two thermal components, a non-thermal component, and a background model. We find that it is critical to include redshifts/blueshifts and broadening of the emission lines in the two thermal components to achieve a reasonable fit, given the high spectral resolution of the Resolve calorimeter. We fit the spectra with two versions of the `AtomDB` atomic database (3.0.9 and 3.1.0) and two versions of the `SPEX` (3.08.00 and 3.08.01*) spectral fitting software. We report the significant differences in the fitted parameters so that users might understand which results are sensitive to the atomic data version. Overall we find good agreement between `AtomDB` 3.1.0 and `SPEX` 3.08.01* for the spectral models considered in this paper. The most significant difference we found between `AtomDB` 3.0.9 and 3.1.0 and between `AtomDB` 3.1.0 and `SPEX` 3.08.01* is the Ni abundance, with the new atomic data favoring a considerably lower (up to a factor of 3) Ni abundance compared with the previous versions. Both regions exhibit significantly enhanced abundances compared to Solar values, indicating that supernova ejecta dominate the emission in these regions. We find that the abundance ratios of Ti/Fe, Mn/Fe, and Ni/Fe are significantly lower in the north-west than the south-east, with the Ti/Fe and Mn/Fe ratios consistent with zero in the north-west. These different abundance ratios from regions on opposite sides of the remnant strengthen the case for an asymmetric explosion of the progenitor. We describe the semi-empirical models that were developed and suggest that they might be useful in the calibration of moderate spectral resolution instruments.

Keywords: ISM: individual objects (Cassiopeia A) — ISM: supernova remnants — shock waves — supernovae: individual (Cassiopeia A)

1 Introduction

Cassiopeia A (Cas A) is the youngest known core-collapse supernova remnant (SNR) in the Galaxy with an estimated age of ∼350 yr (Thorstensen et al. 2001; Fesen et al. 2006) and a distance of ∼3.4 kpc (Reed et al. 1995). The progenitor has been determined to be a Type IIb supernova (SN) using light echo spectroscopy (Krause et al. 2008; Rest et al. 2011) with an estimated mass of 15–25 $M_{\odot}$ (Chevalier & Oishi 2003; Hwang & Laming 2012; Lee et al. 2014). The ejecta mass has been estimated to be ∼3 $M_{\odot}$ (Laming & Hwang 2003), of which the majority has been heated by the reverse shock to X-ray emitting temperatures (DeLaney et al. 2014; Laming & Temim 2020). The ejecta structure is asymmetric as the Fe ejecta are at larger radii from the presumed explosion center than the Si ejecta in some regions (Hughes et al. 2000; Sato et al. 2021; Tsuchioka et al. 2022)

Received: 2025 May 29; **Accepted:** 2025 July 30

and the Ti and Fe ejecta have strikingly different spatial distributions (Grefenstette et al. 2014). The prominent jet-like structures in the north-east and south-west, seen in optical and X-ray (Fesen & Milisavljevic 2016; Hwang et al. 2004), also indicate an asymmetric explosion. Three-dimensional (3D) hydrodynamical models of a neutrino-driven SN explosion are able to reproduce the asymmetric morphology of the ejecta (Orlando et al. 2016, 2021, 2022), both the ring-like spatial structures and the inversion of the high-$Z$and low-Z material.

Cas A has the highest X-ray flux in the 2.0–10.0 keV bandpass of any Galactic SNR with a spectrum dominated by thermal emission. The X-ray spectrum contains bright lines of Mg, Si, S, Ar, Ca, Fe, and Ni (Willingale et al. 2002), produced both by ejecta heated by the reverse shock (Hwang & Laming 2012) and by circumstellar material heated by the forward shock (Vink et al. 2024). Although the thermal component dominates the overall flux, the non-thermal component is a significant contributor (Helder & Vink 2008) and has been shown to vary on time-scales of years (Patnaude et al. 2011; Uchiyama & Aharonian 2008). The energy shifts of the bright Si K, S K, and Fe K lines have been used to construct maps of the Doppler velocities (Willingale et al. 2002; Lazendic et al. 2006; DeLaney et al. 2010), with values ranging from -2500 to $+4000\,\mathrm{km\,s^{-1}}$, to explore the 3D structure of the remnant. These maps show a structure in the Fe K emission that is predominantly blueshifted in the south-east (SE) and predominantly redshifted in the north-west (NW). The Si K and S K emission show a similar pattern of blueshifts and redshifts between the SE and NW, but with a more complicated structure—possibly indicating that more velocity components are present for Si and S. Studies of the optically emitting ejecta (Milisavljevic & Fesen 2013) reveal a torus-like geometry tilted at 30° with respect to the plane of the sky with velocities ranging from -4000 to $+6000\,\mathrm{km\,s^{-1}}$. Cas A exhibits a complex morphology with multiple plasmas with different conditions (temperature, density, elemental abundance, ionization time-scale, velocity, etc.) contributing to the X-ray emission along any given line of sight.

Cas A is an appealing target for high-resolution X-ray spectroscopy because of its high flux and line-rich spectrum. The X-ray Imaging and Spectroscopy Mission (XRISM; Tashiro et al. 2020, 2024, 2025) launched on 2023 September 7, carrying two instruments for X-ray observations. One instrument, called Resolve (Ishisaki et al. 2022; Porter et al. 2024), is an X-ray calorimeter array with 36 pixels arranged in a 6×6 array covering $3' \times 3'$ on the sky that provides high-resolution, non-dispersive spectroscopy—full-width at half maximum (FWHM) ∼4.5 eV at 6.0 keV—in the 1.5–12.0 keV bandpass. The other instrument, called Xtend (Mori et al. 2022; Uchida et al. 2025; Noda et al. 2025), is a charge-coupled device (CCD) instrument with a large field of view ($38\farcm5 \times 38\farcm5$) that provides moderate resolution spectroscopy in the 0.4–13.0 keV bandpass. The XRISM X-ray Mirror Assembly (XMA) has an angular resolution of $1\farcm3$ half-power diameter (HPD) and $8''$ FWHM. The Resolve instrument provides unprecedented spectral resolution for diffuse emission and extended objects, representing a major advance over the CCD and gratings instruments on the Chandra X-ray Observatory and XMM–Newton.

The XRISM observations of Cas A were planned with various objectives that exploit the power of non-dispersive, high-resolution spectroscopy. The use of the energy shifts of the bright lines/line complexes of Si, S, Ar, Ca, Fe, and Ni was proposed in order to reveal the velocity structure of the remnant to a level of precision that had not been possible with previous observations. The high spectral resolution of Resolve allows the broadening of the bright lines to be measured to further constrain the 3D structure and the conditions of the plasma, specifically the ion temperature. The high-quality data from Resolve also allow an exploration of the differences between the He-like emission (the Heα triplets) and H-like emission (the Lyα lines) of Si and S, by spectroscopically resolving different regions behind the shock front with different plasma conditions. The use of the high sensitivity of Resolve was proposed in order to detect and characterize relatively weak emission lines from the odd-Z elements of P, Cl, and K. This enables a comparison with SNe nucleosynthesis models in order to constrain the properties of the progenitor and the explosion. Several papers have been prepared on these topics and three are included in this special issue: Suzuki et al. (2025) present the dynamics of Si and S, making use of the H-like and He-like lines; Bamba et al. (2025) present the velocity and broadening of the Fe K complex; and Vink et al. (2025) present maps of the Si and S velocities. A search for emission from the odd-Z elements of P, Cl, and K is described by XRISM Collaboration (2025), and their paper has been submitted to another journal. This paper serves as an introduction to the XRISM observations of Cas A, and we discuss some technical aspects of the analysis.

All of these results depend upon the high spectral resolution and the calibration of the Resolve instrument. They also depend upon the spectral models that are used to interpret the high-resolution data. In this paper, we focus on the spectral models and how the results depend upon these models. We compare results for two of the brightest regions in Cas A that were observed on-axis with two plasma emission models, the `APEC` software/`AtomDB` database (Foster et al. 2012) and the `SPEX` software (Kaastra et al. 1996). Futhermore, we compare results with the versions of these software packages and associated atomic databases that were available before and after the launch of the XRISM. Some of the changes in the software and databases were motivated by the high-resolution spectra from Resolve, in particular the spectra from Cas A. We describe which of the model parameters are affected by these changes.

This paper is organized as follows. In section 2, we describe the XRISM observations of Cas A and the processing of the data relevant for this analysis. In section 3, we present the image analysis, maps of the spatial–spectral mixing effect, and the spectral analysis with `AtomDB` and `SPEX`. In section 4, we discuss the results of the spectral fitting and the comparison of the spectral models. All uncertainties presented in this paper are 1.0σ uncertainties unless specified otherwise.

2 Observations and data reduction

XRISM observed Cas A twice during the Performance Verification (PV) phase, from 2023 December 11 to 14, targeting the SE region (ObsID 000129000) and from 2023 December 14 to 17, targeting the NW region (ObsID 000130000). The nominal aim point, roll angle, and accepted Resolve exposure times for both observations are listed in table 1. The observations were made with the Resolve dewar gate valve closed, which restricted the bandpass to energies above ∼1.5 keV.

Table 1. XRISM observation log of Cas A.

ObsID	RA (J2000.0)	Dec (J2000.0)	Roll (°)	Start date date	Exposure* (ks)
000129000	350.930	+58.808	258.52	2023345.243	181.3
000130000	350.862	+58.822	254.06	2023348.584	165.7

*Accepted Resolve exposure after applying standard filtering criteria.

The observation data were processed using the pre-pipeline software version `004_001.15Oct2023_Build7.011` and the processing (pipeline) script `03.00.011.008`. The Resolve detector gain was calibrated on-orbit using 55 fiducial gain measurements (29 for SE and 26 for NW) of ^{55}Fe radioactive sources during Earth's occultation, achieving an energy resolution of 4.55 ± 0.02 eV (FWHM) and 4.53 ± 0.02 eV (FWHM) at 5.9 keV for SE and NW, respectively (Porter et al. 2024). The energy-scale error using the constantly illuminated calibration pixel was 0.23 and 0.31 eV for SE and NW, respectively, which is comparable to other XRISM observations. In this early observation, the fiducial gain measurements were made more frequently, enabling precise gain tracking of all pixels. Thus we include pixel #27 (see figure 2 for the pixel numbering scheme), which has been shown to exhibit erratic gain jumps, and we perform the analysis using the full array for both observations.

The Resolve data for both observations were reprocessed with the HEASoft 6.34 software package, applying calibration from XRISM CalDB 9 (Version 20240815). The default screening as described in the XRISM team's analysis of N 132D (XRISM Collaboration 2024) was applied, resulting in clean exposure times of 181.3 and 165.7 ks for SE and NW, respectively. We do not apply any additional good time interval (GTI) screening based on the pointing stability of the satellite. Only high-resolution primary ("Hp" or `ITYPE=0`) grade events were included for the following analysis, as they account for more than 96% of the 2–10 keV events in each observation. A redistribution matrix file (RMF) was generated in extra large (XL) size in split-RMF format by the `rslmkrmf` task using the cleaned event files. This RMF incorporates: Gaussian core, low-energy exponential tails, Si fluorescence lines, escape peaks, and electron loss continuum. The ancillary response file (ARF) was constructed with `xaarfgen` task, using an exposure-corrected Chandra image in the 0.5–5 keV band as an input model for source flux. A non-X-ray background (NXB) spectrum was modeled from a database[1] of Resolve night-Earth data using `rslnxbgen`, while the sky background was ignored. The spectra were binned using `SPEX v3.08.01` software package applying the optimal binning method of Kaastra and Bleeker (2016) where each bin had at least one count to fit the spectra using the C-statistic (Cash 1979) for the fits performed in `SPEX`, and were binned with the `ftool ftgtoupha` with the optimal binning option for the fits performed in `XSPEC`.

3 Analysis and results

3.1 Image analysis

3.1.1 Xtend and Resolve images

Figure 1 shows the Xtend image of Cas A in the 1.5–10.0 keV band from the SE and NW observations in the left panel. The Xtend data cover all of Cas A and the surrounding regions due to its large FOV. This image has been extracted from those data to show only the region around Cas A. The Xtend image shows the familiar partial shell-like structure of Cas A known from the Chandra, XMM, and earlier observations, with the bulk of the emission arising from the shock-heated ejecta. The two Resolve FOVs are overplotted on the Xtend image, as shown by the dashed white squares. The Resolve images are shown in the right panel of figure 1. Both images present the counts ks^{-1} in a pixel in the 1.5–10.0 keV band, indicating the statistical quality of the data for spectroscopy. Note that the calibration pixel (pixel #12) in the upper-left corner is omitted from the white square because it contains no data from the remnant. Figure 2 shows the pixel numbering scheme for the two Resolve pointings overplotted on the Chandra true-color image and the definition of the super-pixels "a–i" that will be used in sub-subsection 3.2.2. The super-pixels are simply 2 × 2 pixel regions, except for super-pixel "a" which is missing one of the four pixels, pixel #12.

The SE pointing was positioned to maximize coverage of the previously known Si-rich and Fe-rich regions. The NW pointing was positioned to cover most of the arc of emission in the west, part of the bright arc in the north (which is also rich in Si and Fe), and the region towards the center that is apparently interacting with the shell of circumstellar medium (CSM) material. The Xtend image shows the parts of the remnant that are outside the Resolve FOV. Regions that are outside of, but close to, the Resolve FOV will contribute significantly to the observed counts, as discussed in detail in subsubsection 3.1.2. The Xtend and Resolve images both show that spatial differences can be observed even with the moderate angular resolution of XRISM.

3.1.2 Spatial–spectral mixing

The in-orbit on-axis point spread function (PSF) of XRISM is 1.′3 half-power diameter (HPD) (Hayashi et al. 2024), which is relatively large compared to the Resolve pixel size of 0.′5. This leads to photons from neighboring regions cross-contaminating the Resolve pixel spectra. Given that this happens at all energies and a Resolve spectrum is associated with each spatial pixel, this mixing affects the Resolve spectrum both spatially and spectrally, and is thus referred to as spatial–spectral mixing (SSM). In addition to the effects of the PSF, small wobbles in the XRISM attitude can also result in SSM. As these can affect the physical parameter mapping of extended sources, we want to estimate their severity using simulated data.

We implemented an algorithm based on Monte Carlo simulations to convolve the data from X-ray missions with better spatial resolution (e.g. Chandra or XMM) to the XRISM response. We take an event file and perform Monte Carlo simulations on the sky location of each photon by drawing from the cumulative distribution functions (CDFs) of the PSF and the attitude profiles. The XRISM PSF varies with photon energy and off-axis angle, and has a complex shape due to mirror support structures, imperfect alignments, and non-ideal foil surfaces. However, for our analysis, we used the on-axis PSF from the encircled energy function (EEF) for 4.5 keV photons, thus assuming an energy-independent and azimuthally symmetric PSF. To account for attitude effects, we used the distribution of aim-point offsets (separately for RA and Dec) after applying the GTI correction. The early PV observations of Cas A were performed

[1] ⟨https://heasarc.gsfc.nasa.gov/docs/xrism/analysis/nxb/index.html⟩.

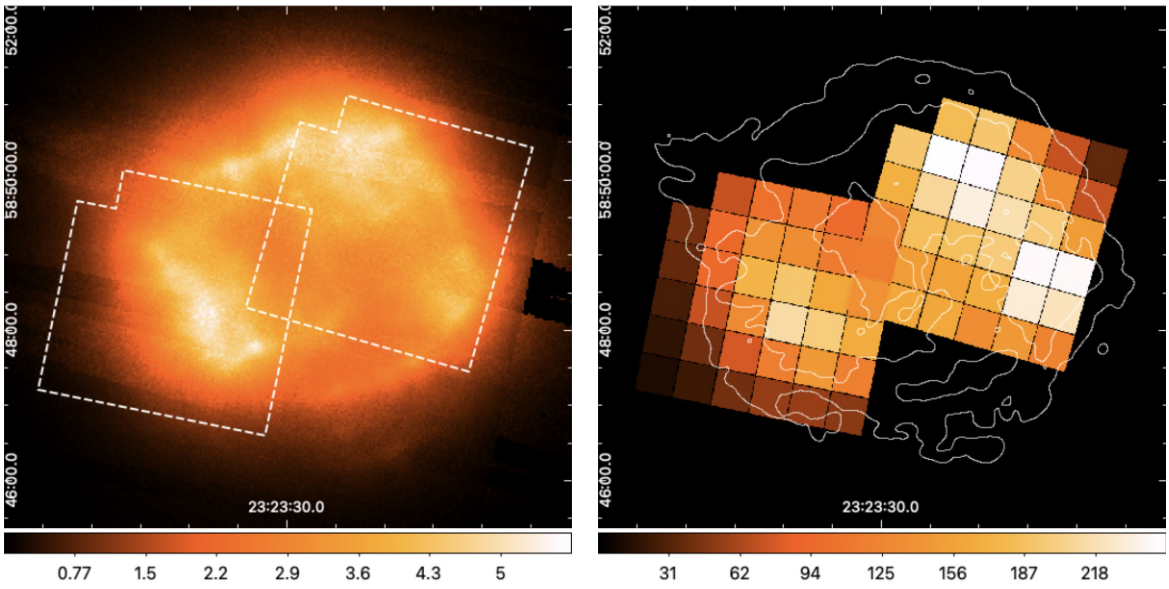

Fig. 1. Left: Xtend counts image from the SE and NW pointings in the 1.5–10.0 keV band. The Resolve FOVs are indicated by the dashed white squares. The data have been exposure corrected and the units are counts ks^{-1} in a pixel. Right: Resolve counts images from the SE and NW pointings in the 1.5–10.0 keV band. The individual pixels in the array are indicated by the small black squares. The data have been exposure corrected and the units are counts ks^{-1} in a pixel. The contours show Cas A as derived from a broad-band image of a Chandra observation (ObsID 4638).

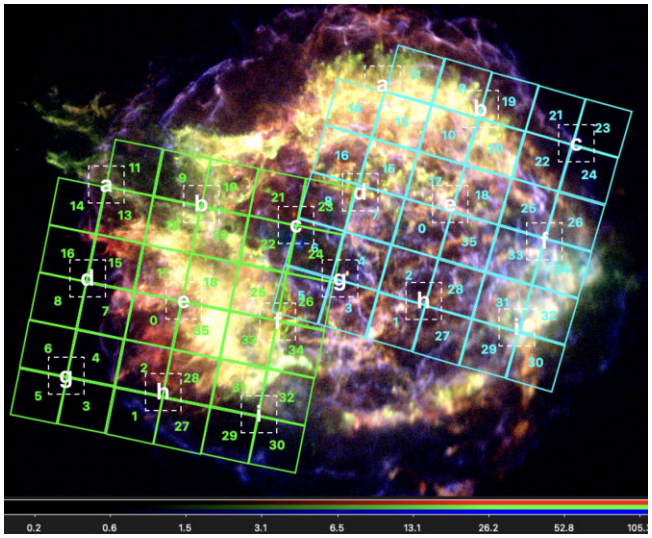

Fig. 2. Resolve pixel arrays overplotted on the Chandra true-color image with the individual pixels numbered 0–35 and the super-pixels labelled a–i.

before the ground software update that refined the Earth occultation prediction for the star trackers under specific attitude and orbit conditions. During these observations, the attitude and orbit control system relied on the inertial reference units for longer periods. The resulting attitude variations were therefore larger than those in later observations, and no other scientific observations were affected by this issue. Figure 3 shows the GTI-corrected pointing offset for the the SE observation and the corresponding CDFs that are used to perform the Monte Carlo simulation.

We used the 2009 Chandra observation of Cas A (ObsID 4638) with an exposure time of 160 ks and a total photon count of ∼50 million. We only considered photons in the energy range 1.8–7 keV, as this bandpass overlaps with that of Resolve, which accounts to ∼23 million photons, and we ignored the background. The Chandra sky coordinates of a photon are considered as its "true" sky location, and then an offset (separately for RA and Dec) is added to account for the SSM. Because we know the sky location of the photon before and after the convolution, we can precisely track back the photons from the detector plane to their origin on the sky. Figure 4 shows the true sky location of the photons that are eventually detected at Resolve pixel #0 (marked with a red border); the left panel accounts for only PSF effects, and the right panel shows attitude effects for the SE observation alone. We estimate that ∼80% of the photons originate from outside the sky region covered by Resolve pixel #0 due to just PSF effects, and ∼50% due to attitude effects alone. When both effects are considered, only ∼6% of the photons come from the sky region covered by pixel #0—we refer to this as the purity percentage. Figure 5 shows maps of the purity percentage per pixel and per 2 × 2 pixel region for the SE observation. The two leftmost images show the purity percentage maps for photons in the energy range 1.8–3 keV, and the two rightmost images show maps for the 4–7 keV range. In addition, we also estimate the contribution from other pixel regions. For example, in the case of Resolve pixel #0, the majority of photons (∼27%) originate from the sky region corresponding to Resolve pixel #35. This cross-contamination between pixels (i.e., internal SSM) can be used to account for SSM while spectral fitting. Figure 6 shows the cross-contamination percentages in the SE and NW observations for 2 × 2 Resolve pixel regions (the so-called super pixels), which are labeled `a` to `i` as indicated in figure 2. The diagonal of the matrix in figure 6 is the same as a purity percentage map. We find that the highest purity percentage for Cas A observations for individual pixels is ∼30% and increases to ∼50% when using regions of 2 × 2 pixels. We also evaluate the external SSM (i.e., the contribution of photons from outside the Resolve FoV) as ∼24% and ∼22% for the SE and NW observations, respectively.

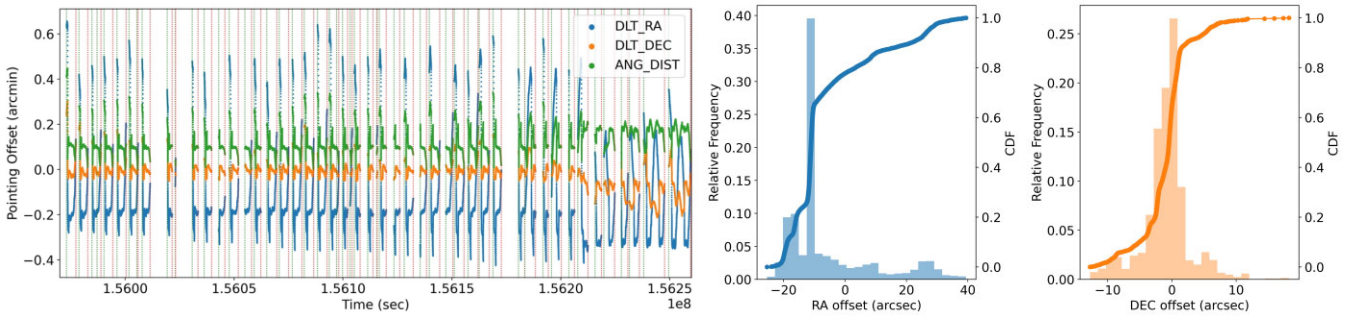

Fig. 3. XRISM pointing stability during the SE observation of Cas A. The left panel shows the pointing offset after applying the GTI correction. The blue (DLT_RA) and orange (DLT_DEC) lines show the offset in RA and Dec, respectively, and ANG_DIST shows the net angular distance from the nominal pointing (RA_NOM, DEC_NOM). The green and red dotted lines show the GTI start and stop time, respectively. The two panels on the right show the distribution of offset in RA and Dec, and the corresponding CDFs, which are used in a Monte Carlo approach to convolve the photon sky locations to account for attitude effects.

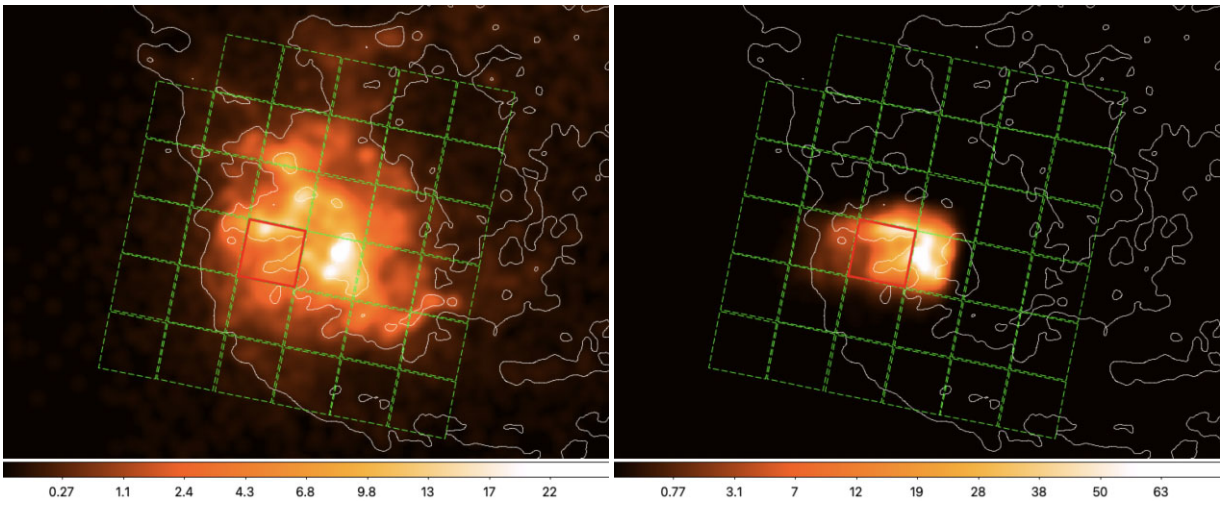

Fig. 4. Sky location of all the photons in the energy range 1.8–7 keV that are detected at the Resolve pixel #0 (marked with a red border). The dashed green boxes outline the Resolve pixel array for the SE observation. The left panel shows the effects due to the relatively large PSF of XRISM and the right panel shows the blending due to the attitude effects alone. The images are smoothed with a Gaussian kernel to represent the small variation over different Monte Carlo simulation runs. The white contours are from a Chandra broad-band image. The photon counts are shown with a square root scale.

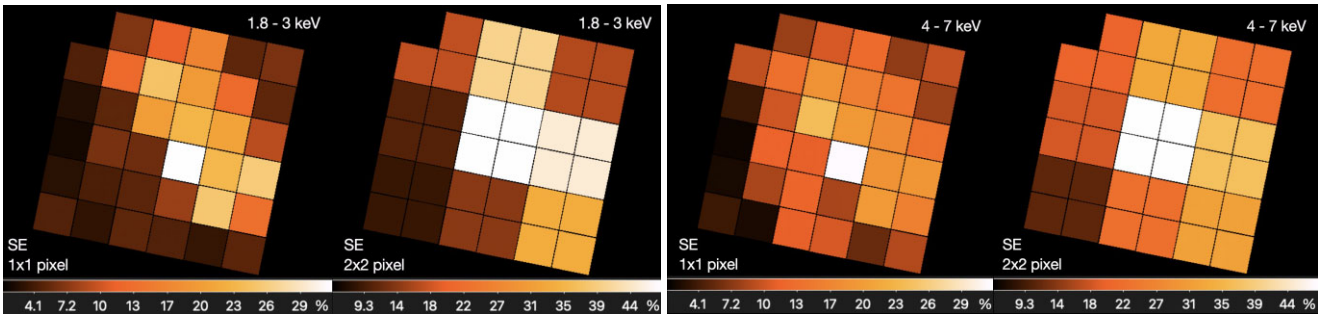

Fig. 5. Percentage of photons detected at a Resolve pixel that actually originate from the corresponding sky region. These purity maps are shown for the SE observation for each Resolve pixel and 2 × 2 pixel regions. The left two panels show the purity percentage of photons in the energy range 1.8–3 keV and the right two panels are for the energy range 4–7 keV.

3.2 Spectral analysis

3.2.1 Integrated spectra from each observation

Spectra were extracted from all pixels, except for the calibration pixel #12, to create an integrated spectrum for each observation (SE and NW) using the HEASoft tool XSELECT. These two spectra are plotted in the left panel of figure 7, with the SE spectrum in blue and the NW spectrum in red. These spectra are dominated by the bright line complexes of Si, S, Ar, Ca, Fe, and Ni, with many weaker lines evident in the spectra. It is important to note that these spectra are derived from a mixture of multiple regions within the remnant, each with its own plasma conditions (temperature, ionization time-scale,

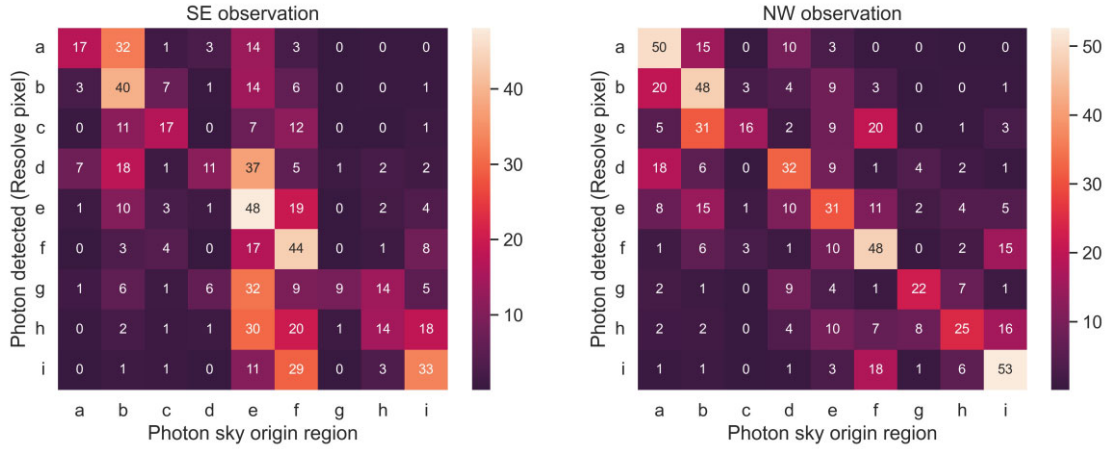

Fig. 6. Estimated photon (in the energy range 1.8–7 keV) cross-contamination percentage for Resolve 2 × 2 pixel regions. This shows the extent of internal SSM for the SE and NW observations by accounting for both PSF and attitude effects. The regions labeled a to i are marked in figure 7. The color bar is in units of percentage.

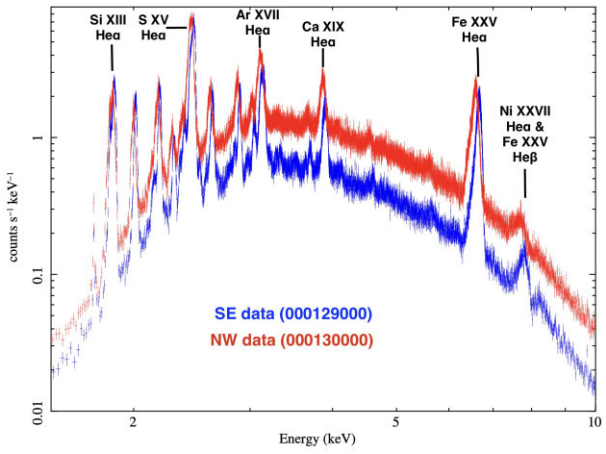

Fig. 7. Resolve spectra from the entire array from the SE pointing (blue) and the NW pointing (red). The prominent line complexes of Si, S, Ar, Ca, and Fe are labeled. The redshift/blueshift between the observations is apparent.

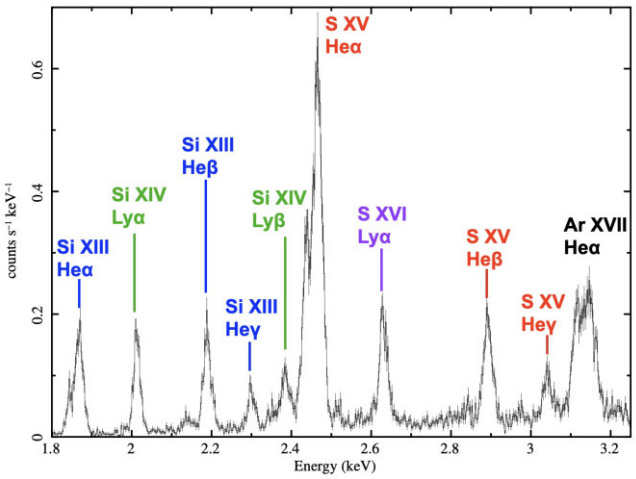

Fig. 8. Resolve spectra from pixel #35 in the SE pointing. The line complexes of Si XIII, Si XIV, S XV, S XVI, and Ar XVII are labeled.

abundances, etc.) and velocity structure as described in subsubsection 3.1.2. This mixing of emission from different regions broadens the lines significantly beyond the resolution of the Resolve calorimeter, complicating efforts to measure the intrinsic thermal broadening. Even with this large degree of mixing and the associated broadening, it is clear that there is a systematic energy shift between these two spectra. The SE spectra are blueshifted with respect to the NW spectrum. This is the same blueshift/redshift pattern from SE to NW in the remnant that has been observed in earlier observations of Cas A (Markert et al. 1983; Holt et al. 1994; Willingale et al. 2002; Lazendic et al. 2006).

Spectra extracted from single pixels or small groups of adjacent pixels have significantly less broadening than the spectra extracted from the entire array. A map of the Resolve pixels over-plotted on the Chandra image of Cas A is shown in figure 2. The individual pixels are numbered in this image and groups of 2 × 2 super pixels are labeled a–i. To more clearly demonstrate the spectral resolving power of the calorimeter, we extracted a spectrum from a single pixel, pixel #35 in the SE pointing that has the highest purity, as shown in figure 5. Figure 8 displays this spectrum showing that the Si XIII and S XV Heα, Heβ, Heγ, the Si XIV Lyα and Lyβ, the S XVI Lyα, and the Ar XVII Heα lines/line complexes are cleanly resolved. There is also an S XVI Lyβ line that is blended with the forbidden line of the Ar XVII Heα triplet because the energies of these lines only differ by ∼2 eV. This spectrum demonstrates the power of the Resolve calorimeter to perform high-resolution spectroscopy in this energy range even with the XRISM Gate Valve closed. The broadening of the lines in the spectrum from a single pixel is significantly less than that in the spectra from the entire array. This can be seen in figure 8 as the forbidden and resonance lines of the S XV Heα triplet are resolved from each other. The three companion papers in this issue (Bamba et al. 2025; Suzuki et al. 2025; Vink et al. 2025) measure the energy shifts and the broadening of these lines/line complexes to characterize the plasma conditions and the 3D structure of Cas A, taking advantage of the high spectral resolution and precise gain calibration of the Resolve calorimeter.

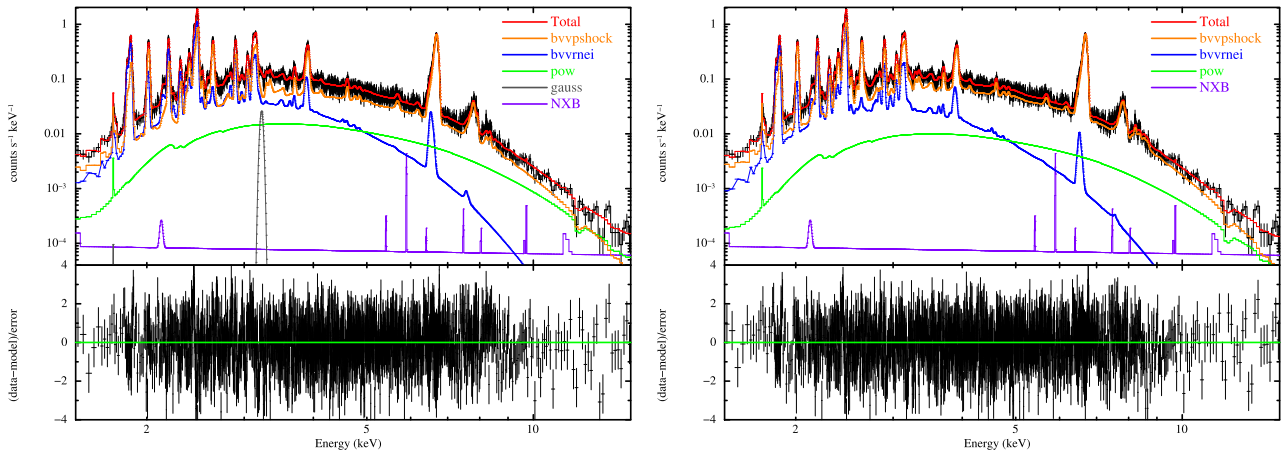

Fig. 9. Left: Resolve spectra from the on-axis point, so-called super-pixel "e" for the SE pointing in the 1.5–15.0 keV range, fit with XSPEC and AtomDB 3.0.9. Right: Resolve spectra from the on-axis point, super-pixel "e" for the SE pointing in the 1.5–15.0 keV range, fit with XSPEC and AtomDB 3.1.0. The data are represented by the black data points and have been rebinned for display purposes only. The upper red curve is the total model, the orange curve is the high kT bvvpshock component, the blue curve is the low kT bvvrnei component, the green curve is the power-law component, the gray line at ∼3.2 keV is the additional Gaussian component, and the purple curve is the NXB component. The residuals are plotted in the lower panel.

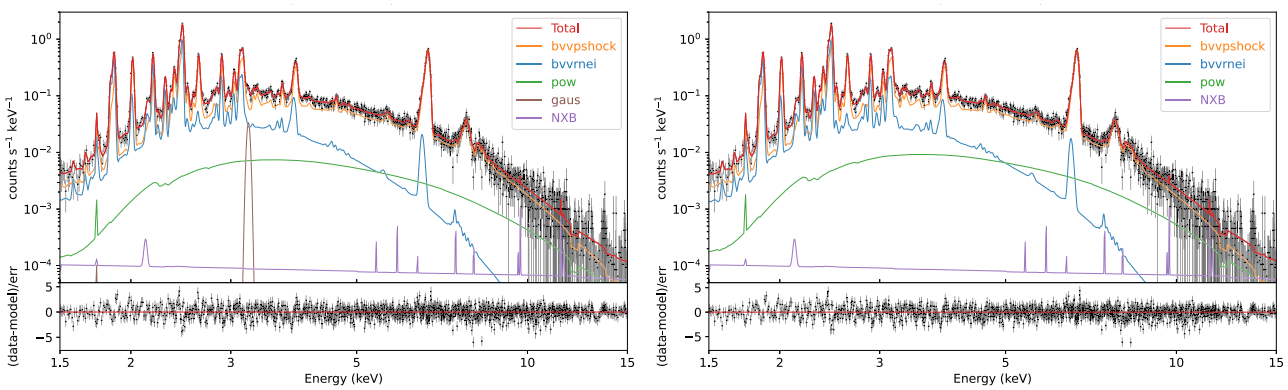

Fig. 10. Left: Resolve spectra from the on-axis point, so-called super-pixel "e" for the SE pointing in the 1.5–15.0 keV range, fit with SPEX 3.08.00. Right: Resolve spectra from the on-axis point, super-pixel "e" for the SE pointing in the 1.5–15.0 keV range fit with SPEX 3.08.01*. The data are represented by the black data points. The upper red curve is the total model, the orange curve is the high kT bvvpshock component, the blue curve is the low kT bvvrnei component (the SPEX equivalent model is called neij), the green curve is the power-law component, the brown line at ∼3.2 keV is the additional Gaussian component, and the purple curve is the NXB component. The residuals are plotted in the lower panel.

3.2.2 Spectra from bright, on-axis regions

We extracted spectra from the on-axis, 2 × 2 pixel, region labeled as super-pixel "e" in figure 2 from both the SE and NW observations. These 2 × 2 pixel regions have a relatively high purity of counts arising from these parts of Cas A, as described in sub-subsection 3.1.2, and are not affected by uncertainties in the off-axis mirror response. The on-axis mirror response should have the smallest uncertainties at this point in the mission. However, it is worth noting that a significant amount of the flux in these regions arises from the adjacent regions, as the purity values are ≈48% and ≈31% for the SE and NW spectra, respectively. Nevertheless, these spectra should exhibit significantly less broadening due to the mixing of emission from different regions, as described in sub-subsection 3.2.1 and as shown in figures 3 and 8 in Vink et al. (2025). The SE spectrum is shown in figures 9 and 10 and the NW spectrum is shown in figures 11 and 12 in the 1.5–15.0 keV band. The spectral models are described in detail in sub-subsection 3.2.3. The SE and NW pixel "e" spectra are similar in that the lines of Si, S, Ar, Ca, Fe, and Ni dominate the flux but the relative contribution of the lines compared with the continua components is different between the two spectra. The line emission is relatively stronger in the SE spectrum than in the NW spectrum. The Si and S lines appear to be narrower than in the spectrum from the entire array shown in figure 7 but the Fe K emission appears to be relatively broad. The features around the Ni XXVII Heα triplet and the Fe XXV Heβ lines at ∼7.8 keV appear weaker relative to the Fe XXV Heα triplet in the NW spectrum compared with the SE spectrum. These similarities and differences are discussed in subsection 4.1.

3.2.3 Spectral models

Initial fits with a single thermal, non-equilibrium ionization (NEI) model showed that it was not possible to fit the line emission from Si to Fe with such a model. We used the vvrneimodel in XSPEC (Arnaud 1996), which assumes that the plasma starts in collisional ionization equilibrium at an initial temperature specified by the user and a single ionization time-scale. Depending on the value of the initial

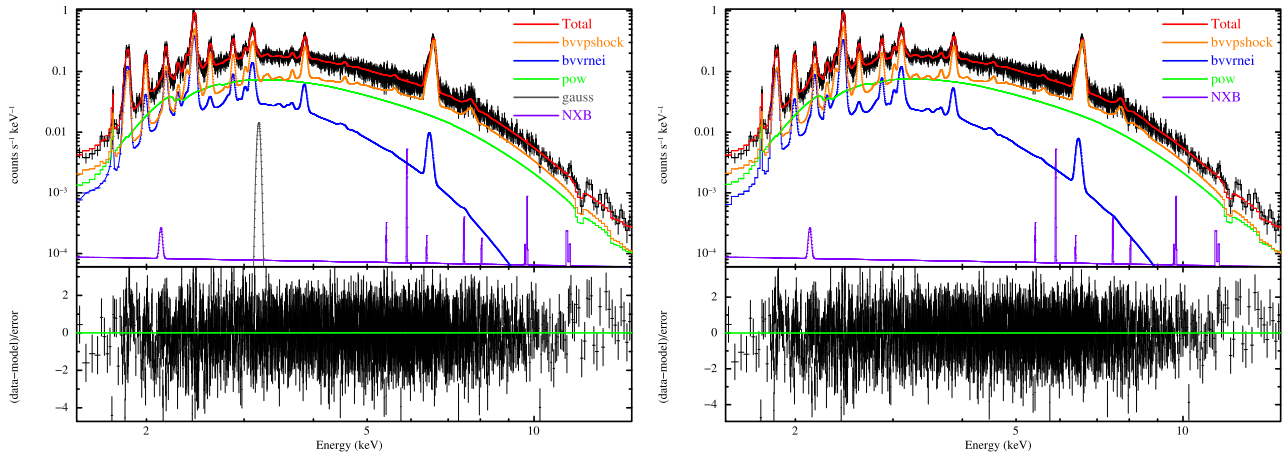

Fig. 11. Left: Resolve spectra from the on-axis point, so-called super-pixel "e" for the NW pointing in the 1.5–15.0 keV range fit with XSPEC and AtomDB 3.0.9. Right: Resolve spectra from the on-axis point, super-pixel "e" for the NW pointing in the 1.5–15.0 keV range fit with XSPEC and AtomDB 3.1.0. The data are represented by the black data points and have been rebinned for display purposes only. The upper red curve is the total model, the orange curve is the high kT bvvpshock component, the blue curve is the low kT bvvrnei component, the green curve is the power-law component, the gray line at ∼3.2 keV is the additional Gaussian component, and the purple curve is the NXB component. The residuals are plotted in the lower panel.

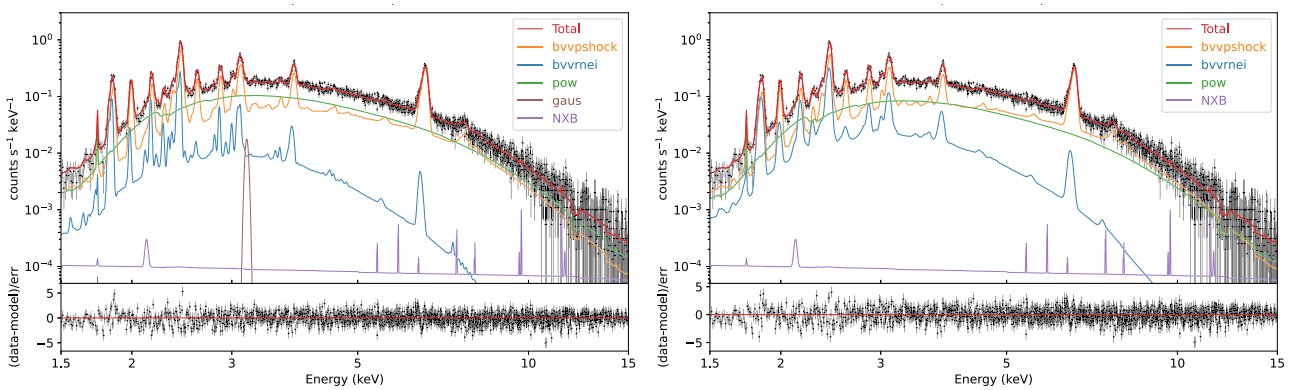

Fig. 12. Left: Resolve spectra from the on-axis point, so-called super-pixel "e" for the NW pointing in the 1.5–15.0 keV range fit with SPEX 3.08.00. Right: Resolve spectra from the on-axis point, super-pixel "e" for the NW pointing in the 1.5–15.0 keV range fit with SPEX 3.08.01*. The data are represented by the black data points. The upper red curve is the total model, the orange curve is the high kT bvvpshock component, the blue curve is the low kT bvvrnei component (the SPEX equivalent model is called neij), the green curve is the power-law component, the brown line at ∼3.2 keV is the additional Gaussian component, and the purple curve is the NXB component. The residuals are plotted in the lower panel.

temperature that is specified, this model can represent a recombining or ionizing plasma. Fits with two (vvrnei) components improved the fit but could not represent the broadening of the lines. Fits with two broadened NEI models (bvvrnei) improved the fit significantly but there were still large residuals around the Fe xxv Heα triplet, given its asymmetric profile. We then substituted a bvvpshock model for one of the bvvrnei components. A bvvpshock model is a constant temperature, plane-parallel shock model that takes into account the distribution of ionization time-scales. The addition of a bvvpshock model provided a significantly improved fit to the Fe xxv Heα triplet because it integrates the emission over a range of ionization time-scales at a single temperature. This can produce emission at lower charge states than Fe xxv depending on the temperature and ionization time-scale, and can fill in the energy range just below the peak of the Heα triplet. Based on these results, we selected a two-component model consisting of a bvvrnei component to provide most of the emission at low energies and a bvvpshock component to provide most of emission at high energies, with both components contributing significantly in the middle of the band. We allowed the abundances of Mg, Si, P, S, Cl, Ar, K, Ca, Ti, Cr, Mn, Fe, and Ni to vary. Abundances of elements with a lower atomic number than Mg and abundances of Al, V, Co, Cu, and Zn were frozen at the solar value. We adopt the solar abundance values of Lodders, Palme, and Gail (2009) for all of the fits in this paper. For the XSPEC fits, we set the parameter APECBROADPSEUDO such that the low-flux lines were also broadened. A similar effect was accomplished in the SPEX fits by broadening all the lines in the model. The non-thermal emission was represented by a single power-law component. The NXB was modeled using the template developed by the XRISM calibration team and normalized to the flux in the 13.0–15.0 keV band. The NXB template consists of a power law with an index of 0.16 and 17 Gaussians for the instrumental lines. The absorption due to the intervening interstellar medium (ISM) was modeled using the phabs component. We also included a Gaussian component because fits with the pre-launch versions of AtomDB and SPEX did not include sufficient emission around an energy of ∼3.2 keV to

account for a line-like feature. The final model we used to fit the SE and NW spectra consisted of an absorption component (phabs), two thermal components (a bvvrnei and a bvvpshock), one non-thermal component (powerlaw), a Gaussian, and the NXB component.

Detailed fits with this model provided reasonable fits to both data sets across the relatively broad band of 1.5–15.0 keV but revealed significant degeneracies among some of the parameters. We started the fits with most parameters free to vary but it became clear that we would need to link and/or constrain some of the parameters, otherwise the fits would not converge. We fixed the neutral hydrogen column density ($N_{\rm H}$) to 1.5×10^{22} cm^{-2} as the fits are not sensitive to the absorbing column with the Gate Valve closed. We started the fits with the Mg, Si, P, S, Cl, Ar, K, Ca, Ti, Cr, Mn, Fe, and Ni abundances free for each of the two thermal components. This proved to be too many degrees of freedom for the fits, so we linked the abundances for the two thermal components. The initial temperature of the bvvrnei component was set to 0.080 keV, because we expect the plasma to be ionizing in Cas A, and the lower limit on the ionization time-scale for the bvvpshock component was set to 0. The temperature, ionization time-scale, normalization, redshift, and broadening of each thermal component were allowed to vary separately. The power-law index was set to 2.8 for the SE spectrum and to 3.4 for the NW spectrum, based on the results presented in Helder and Vink (2008). The normalization of the power-law component was allowed to vary. The energy and normalization of the Gaussian component were allowed to vary while the width was frozen at 0.02 keV based on the results of fits in a narrow energy range. Finally, the constant factor for the NXB component was determined by fitting in the 13.0–15.0 keV band and then held fixed to that value when the entire model was fit in the 1.5–15.0 keV range. Fits conducted in this manner yielded reasonable results; however, the calculation of the uncertainties on the parameters revealed a degeneracy between some of the parameters for the two thermal components. Setting the ionization time-scale for the bvvrnei component to 1.0×10^{11} cm^{-3} s removed this degeneracy and allowed the uncertainties to be calculated for the remaining free parameters in the thermal models. This resulted in 25 free parameters for the fits.

4 Discussion

Fits were performed with the versions of AtomDB (3.0.9) and SPEX (3.08.00) that were available before the launch of XRISM to provide a baseline of the state of our knowledge before the XRISM data became available. We then performed fits with the versions of AtomDB (3.1.0) and SPEX (3.08.01*), which were released after the launch partially in response to some of the issues raised by the high-resolution data from Resolve. We used SPEX version 3.08.01 with SPEXACT version 3.08.02, which is the atomic database to be published with the updated SPEX software (3.08.02); hereafter, we refer to it as SPEX 3.08.01*. Fits with both versions of AtomDB were performed with XSPEC version 12.14.1.

SPEX version 3.08.01* introduces significant updates to the atomic database compared with version 3.08.00, including:

(1) **Rydberg series**—calculation of hydrogen-like and helium-like S and Fe ions in the Rydberg series up to $n = 52$;
(2) **updated Li-, Be-, and B-like ions**—more comprehensive inner shell and dielectronic recombination calculations for ions in Li-, Be-, and B- like isoelectronic sequences;
(3) **expanded inner shell lines for low charge states**—a more complete data set of inner shell lines for Cr, Mn, Fe, and Ni up to P-like configurations;
(4) **Doppler broadening**—incorporation of Doppler broadening for the recombination continuum and absorption edges.

AtomDB version 3.1.0 (and subsequent minor updates to 3.1.3, as of the time of writing) included several changes to the underlying atomic data, both improvements and bug fixes, as follows:

(1) **Rydberg series**—calculation of H- and He-like emission for the Rydberg series transitions ($n \rightarrow 1$) for all elements, up to $n = 50$ (previously these data stopped at $n = 10$);
(2) **fix to Kβ from Li-like ions**—inner shell emission from Li-like ions was taken from the literature but not correctly handled, which led to Kβ being completely suppressed in these ions; this has now been corrected for all Li-like ions;
(3) **dielectronic recombination satellite lines**—previously, the satellites of Fe were only in the model for $1s2lnl' \rightarrow 1s^2 2l$ transitions where $n \leq 5$, and these have been augmented by increasing n to 15, and including $1s[3,4]lnl' \rightarrow 1s^2[3,4]l$;
(4) **ionization rates**—the data for ionization were updated from Bryans, Landi, and Savin (2009) to Urdampilleta, Kaastra, and Mehdipour (2017), and, in addition, multiple ionization was added from Hahn, Müller, and Savin (2017).

We compare the results from the different versions of AtomDB and SPEX in subsection 4.1.

4.1 Spectral fit results

Table 2 lists the fit results for the SE super-pixel "e" spectrum with AtomDB 3.0.9 and 3.1.0 and SPEX 3.08.00 and 3.08.01* for the model described above. The spectra and model for the fits with XSPEC and AtomDB are shown in figure 9 and the fits for SPEX are shown in figure 10. We first compare fit results with AtomDB 3.0.9 to those with AtomDB 3.1.0, then the results with SPEX 3.08.00 to SPEX 3.08.01*, and finally the results with AtomDB 3.1.0 to SPEX 3.08.01*.

The fits with AtomDB 3.0.9 and 3.1.0 adequately represent the data across the entire bandpass, as can be seen by the residuals in figure 9, but some of the bright lines have significant residuals. The value of the C-statistic decreases from 3821.5 with 3350 degrees of freedom (DOF) to 3674.5 (3352 DOF) for the fit with AtomDB 3.1.0 compared to 3.0.9, indicating a significantly improved fit with 3.1.0. The DOF are lower for the fit with AtomDB 3.1.0 because the Gaussian at 3.2 keV is not included in that model. Notably, all of the abundances are enhanced significantly compared to solar values. This is consistent with a strong ejecta component contribution to this region of the remnant. The Ar XVII Heα ($\sim$3.1 keV) and Ca XIX Heα ($\sim$3.9 keV) line complexes are also clearly visible in these spectra in addition to the lines from Si, S, Fe, and Ni. The two thermal components both contribute significantly to the Si and S line emission from 1.5–3.0 keV, but the

Table 2. Spectral fit results from the SE pointing on-axis 2 × 2 pixel region with AtomDB and SPEX.

Parameter	AtomDB 3.0.9	AtomDB 3.1.0	SPEX v3.08.00	SPEX v3.08.01*
bvvrnei				
$N_{\rm H}$ ($\times10^{22}$cm^{-2})	1.50	1.50	1.50	1.50
$n_{\rm et}$ ($\times10^{11}$ cm^{-3} s)	1.00	1.00	1.00	1.00
$kT_{\rm init}$ (keV)	0.08	0.08	0.002	0.002
kT (keV)	$1.04^{+0.01}_{-0.01}$	$0.91^{+0.03}_{-0.01}$	$0.98^{+0.01}_{-0.01}$	$0.96^{+0.01}_{-0.01}$
Mg	$3.71^{+0.62}_{-0.42}$	$2.46^{+0.43}_{-0.41}$	$4.47^{+0.41}_{-0.48}$	$4.71^{+0.46}_{-0.46}$
Si	$8.88^{+0.50}_{-0.61}$	$7.46^{+0.45}_{-0.31}$	$8.21^{+0.09}_{-0.08}$	$8.63^{+0.09}_{-0.10}$
P	$13.75^{+1.69}_{-1.63}$	$10.00^{+1.40}_{-1.44}$	$11.70^{+2.58}_{-1.08}$	$11.82^{+1.59}_{-1.55}$
S	$9.64^{+0.49}_{-0.31}$	$8.07^{+0.76}_{-0.34}$	$8.47^{+0.08}_{-0.05}$	$8.88^{+0.18}_{-0.07}$
Cl	$10.92^{+1.35}_{-1.35}$	$10.11^{+1.17}_{-1.15}$	$10.98^{+3.35}_{-0.59}$	$10.90^{+1.25}_{-1.22}$
Ar	$8.52^{+0.22}_{-0.31}$	$7.13^{+0.49}_{-0.30}$	$7.27^{+0.13}_{-0.11}$	$7.63^{+0.86}_{-0.12}$
K	$11.59^{+1.61}_{-1.59}$	$9.41^{+1.34}_{-1.31}$	$11.21^{+7.37}_{-0.48}$	$10.66^{+1.50}_{-1.46}$
Ca	$9.87^{+1.06}_{-0.81}$	$7.87^{+0.57}_{-0.34}$	$8.19^{+0.17}_{-0.15}$	$8.60^{+0.16}_{-0.16}$
Ti	$12.63^{+3.85}_{-3.77}$	$9.93^{+2.99}_{-2.89}$	$8.95^{+2.68}_{-3.72}$	$8.99^{+3.39}_{-3.04}$
Cr	$7.28^{+1.20}_{-1.16}$	$5.45^{+0.88}_{-0.83}$	$6.41^{+0.77}_{-1.13}$	$6.42^{+0.97}_{-0.95}$
Mn	$8.49^{+2.20}_{-2.20}$	$5.55^{+1.44}_{-1.37}$	$7.52^{+1.38}_{-2.37}$	$7.48^{+1.93}_{-1.89}$
Fe	$14.52^{+2.78}_{-1.38}$	$11.01^{+1.60}_{-0.60}$	$10.11^{+0.87}_{-0.65}$	$10.28^{+0.55}_{-0.21}$
Ni	$30.73^{+1.85}_{-2.36}$	$11.65^{+1.34}_{-1.26}$	$9.70^{+0.93}_{-0.80}$	$6.62^{+0.90}_{-0.89}$
Redshift (z) ($\times10^{-3}$)	$-1.68^{+0.11}_{-0.11}$	$-1.40^{+0.10}_{-0.12}$	$-1.15^{+0.01}_{-0.02}$	$-1.17^{+0.01}_{-0.01}$
$\sigma_{\rm v}$ (km s^{-1})	1118^{+21}_{-22}	1074^{+25}_{-24}	1085^{+24}_{-18}	1089^{+21}_{-24}
AtomDB norm ($\times10^{-2}$ cm^{-5})	$3.48^{+0.17}_{-0.48}$	$4.23^{+0.21}_{-0.32}$	$4.33^{+0.06}_{-0.04}$	$4.12^{+0.09}_{-0.09}$
SPEX norm ($\times10^{63}$ m^{-3})	–	–	$6.00^{+0.06}_{-0.05}$	$5.70^{+0.12}_{-0.12}$
bvvpshock				
$n_{\rm et}$ ($\times10^{11}$ cm^{-3} s)	$2.16^{+0.07}_{-0.04}$	$1.88^{+0.04}_{-0.06}$	$2.12^{+0.13}_{-0.06}$	$2.11^{+0.02}_{-0.03}$
kT (keV)	$2.84^{+0.06}_{-0.10}$	$2.79^{+0.06}_{-0.07}$	$2.79^{+0.02}_{-0.03}$	$2.73^{+0.07}_{-0.12}$
Redshift (z) ($\times10^{-3}$)	$-4.48^{+0.07}_{-0.07}$	$-4.35^{+0.04}_{-0.07}$	$-4.77^{+0.23}_{-0.01}$	$-4.67^{+0.02}_{-0.01}$
$\sigma_{\rm v}$ (km s^{-1})	1341^{+16}_{-17}	1322^{+8}_{-16}	1270^{+10}_{-15}	1282^{+12}_{-13}
AtomDB norm ($\times10^{-2}$ cm^{-5})	$1.54^{+0.14}_{-0.13}$	$2.16^{+0.09}_{-0.16}$	$2.09^{+0.01}_{-0.01}$	$2.07^{+0.02}_{-0.22}$
SPEX norm ($\times10^{63}$ m^{-3})	–	–	$2.89^{+0.02}_{-0.01}$	$2.86^{+0.02}_{-0.31}$
Power law				
Index	2.80	2.80	2.80	2.80
AtomDB norm ($\times10^{-3}$) (photons cm^{-2} s^{-1} at 1.0 keV)	$6.07^{+1.41}_{-1.05}$	$4.00^{+1.10}_{-0.44}$	$3.02^{+0.11}_{-0.19}$	$3.76^{+0.15}_{-0.25}$
SPEX norm ($\times10^{42}$) (photons s^{-1} keV^{-1} at 1.0 keV)	–	–	$4.17^{+0.16}_{-0.27}$	$5.19^{+0.21}_{-0.35}$
Gaussian				
E (keV)	$3.22^{+0.04}_{-0.03}$	–	$3.22^{+0.01}_{-0.01}$	–
AtomDB norm ($\times10^{-5}$ photons cm^{-2} s^{-1})	$2.06^{+0.37}_{-0.34}$	–	$2.75^{+0.38}_{-0.35}$	–
SPEX norm ($\times10^{40}$ photons s^{-1})	–	–	$3.80^{+0.52}_{-0.48}$	–
Fit statistics				
C-statistic	3821.5	3674.5	3793.1	3801.4
Degrees of freedom	3350	3352	3437	3439

contribution of the bvvrnei component diminishes with increasing energy such that the bvvpshock component provides most of the emission for the Fe K and Ni K complexes. The power-law component does not become comparable to the thermal continuum until an energy of ∼11 keV. There is overall good agreement between the fitted parameters derived with AtomDB 3.0.9 and 3.1.0, with some notable exceptions. All of the abundances agree to within 2.0σ with some agreeing to within 1.0σ, except for the Ni abundance which differs at the many σ level. The abundances are systematically lower with AtomDB 3.1.0 than with 3.0.9. This is primarily driven by the increase in the normalizations for the two thermal components relative to the power-law component. The normalizations for the bvvrnei and bvvpshock components are 22% and 40% higher with AtomDB 3.1.0, while the normalization for the power-law component is 35% lower. The increase in

the normalizations for the thermal components results in more of the continuum being attributed to the thermal components, which reduces the contrast between the line emission and the continuum emission resulting in lower abundances to explain the line emission. In addition, the temperature and redshift for the bvvrnei component and the ionization time-scale for the bvvpshock component are significantly lower with AtomDB 3.1.0. All other parameters agree at the 1.0σ level, notably the broadening terms for both thermal components, and the temperature and redshift for the bvvpshock component. Of all the parameters, the Ni abundance shows the largest difference between AtomDB 3.0.9 and 3.1.0, decreasing from $30.73^{+1.85}_{-2.36}$ to $11.65^{+1.34}_{-1.26}$. This difference is discussed in more detail in subsection 4.2.

The fits with SPEX 3.08.00 and 3.08.01* likewise represent the data well across the entire bandpass, as can be seen by the residuals in figure 10. The value of the C-statistic increases from 3793.1 (3437 DOF) to 3801.4 (3439 DOF) for the fit with SPEX 3.08.01* compared to 3.08.00, indicating a slightly worse fit with 3.08.01*. There is overall excellent agreement for the fitted parameters derived from the fits with the two versions of SPEX. All of the best-fitting parameters agree within 2.0σ except for the abundances of Si and S, and the redshift for the SPEX equivalent of the bvvpshock component. The Si and S abundances agree at the 3.0σ level but the redshift for the bvvpshock component disagrees at more than the 3.0σ level. The Ni abundance is lower with SPEX 3.08.01* but agrees at the 2.0σ level. The abundances with SPEX 3.08.01* are systematically higher than with 3.08.00. In contrast to the fits with AtomDB, the normalizations for the thermal components are lower with SPEX 3.08.01* and the normalization for the power-law component is higher, resulting in higher abundances for the thermal components. The uncertainties on the redshifts in the SPEX models can be small and sometimes asymmetric. We explored the redshift parameter space for both components in detail and found it to be complex with many local minima. This exploration confirmed the small values of the uncertainties in some cases and the asymmetric nature of the uncertainties in others. The bvvpshock redshift only differs by 2% between the SPEX 3.08.00 and 3.08.01* fits, but given the small uncertainties, this difference is significant.

The differences in the fitted parameters between AtomDB 3.1.0 and SPEX 3.08.01* are perhaps more interesting as they reflect the current state-of-the-art in the knowledge of astrophysical plasma emission models. It should be noted that the number of DOF are different between the AtomDB and SPEX fits due to differences in how the optimal binning algorithm is implemented in ftgrouppha and SPEX. In general, there is good agreement between AtomDB and SPEX for most of the parameters, with a few exceptions. All the abundances agree at the 1.0σ level, except for Mg, Si, and Ni, which agree at the 3.0σ level. As noted previously, the Ni abundance changed significantly between AtomDB 3.0.9 and 3.1.0 but even with that change, the Ni abundance is still 3.0σ different between AtomDB and SPEX. The Mg abundances disagree at more than the 2.0σ level; however, this measurement is based almost entirely on the Mg,XII Lyβ line, which is weak in the observed spectrum due to the closed Gate Valve and confused with the neutral Si line from the detector background. Therefore, the uncertainties on the Mg abundances might be larger than the statistical uncertainties alone, given how low the effective area is at this energy with a possibly larger systematic error and significant contribution from the detector background with its associated systematic error. The normalizations for the bvvrnei, bvvpshock, and power-law components all agree to within 1.0σ for AtomDB 3.1.0 and SPEX 3.08.01*, indicating remarkably good agreement for the overall shape of the spectra. However, there are differences that affect the details of the spectra. The redshifts for the bvvrnei and bvvpshock components differ at the many σ level, again partially due to the relative uncertainties being much smaller for the SPEX spectral fits. The temperatures for the bvvrnei components agree at the 2.0σ level but the ionization time-scales for the bvvpshock components disagree at the many σ level. The broadenings (σ_v) for the bvvrnei and bvvpshock components agree at the 1.0σ and 2.0σ levels, respectively. It is interesting to note that the redshift for the bvvrnei component in the SPEX fit is less negative than the redshift in the AtomDB fit, but the redshift for the bvvpshock component in the SPEX fit is more negative than the redshift in the AtomDB fit. This would have the effect of broadening the lines more in the SPEX fit relative to the AtomDB fit. However, the broadening term for the bvvpshock component in the SPEX fit is less than that in the AtomDB fit. Therefore, it appears that the redshift and broadening are combining in different ways for the SPEX and AtomDB fits to represent the widths of the line features. Overall, the agreement between AtomDB 3.1.0 and SPEX 3.08.01* is quite good for the SE spectrum except for the redshifts and the Ni abundances.

Table 3 lists the fit results for the NW super-pixel "e" spectrum with AtomDB 3.0.9 and 3.10 and with SPEX 3.08.00 and 3.08.01* for the model described above. The spectra and model for the fits with XSPEC and AtomDB are shown in figure 11 and the fits with SPEX are shown in figure 12.

The fits with AtomDB 3.0.9 and 3.1.0 adequately represent the data across the entire bandpass, as can be seen by the residuals in figure 11 and the resulting fit statistic values of the C-statistic of ~4000 with 3423/3425 DOF. The value of the C-statistic only changes by 2.5 between the fits, indicating that they are of equal quality. Notably, the abundances are significantly lower than for the SE spectrum, but they are still enhanced compared to solar except for Mg, Ti, Mn, and Ni. This would be consistent with an ejecta contribution in this region but not as strong as in the SE spectrum and with a different composition. All of the fitted parameters (including the model normalizations) agree to within 1.0σ between AtomDB 3.0.9 and 3.1.0 except for the Ni abundance and the ionization time-scale for the bvvpshock component. The Ni abundance decreases from $3.67^{+0.82}_{-0.85}$ to $1.04^{+0.77}_{-0.74}$, consistent at the 2.0σ level. The ionization time-scale for the bvvpshock component is $1.17^{+0.01}_{-0.03} \times 10^{11}$ cm^{-3} s for AtomDB 3.0.9 and $1.07^{+0.02}_{-0.03} \times 10^{11}$ cm^{-3} s, differing by 9% and consistent at the 2.0σ level. It is possible than there is better agreement between AtomDB 3.0.9 and 3.1.0 for the NW spectrum because the line emission is relatively weaker compared with the continuum than in the SE spectrum, and therefore the model for the line emission does not contribute as much to the fit statistic.

The fits with SPEX 3.08.00 and 3.08.01* show a larger variation between the fitted parameters, as can be seen in table 3. The C-statistic is marginally higher, 4049.2 versus 4041.5, for 3.08.01* compared to 3.08.00. There are several parameters that disagree at more than the 2.0σ level between these two fits. Most notable among these are the redshift,

Table 3. Spectral fit results from the NW pointing on-axis 2 × 2 pixel region with AtomDB and SPEX.

Parameter	AtomDB 3.0.9	AtomDB 3.1.0	SPEX v3.08.00	SPEX v3.08.01*
bvvrnei				
N_H ($\times 10^{22}$ cm^{-2})	1.50	1.50	1.50	1.50
n_{et} ($\times 10^{11}$ cm^{-3} s)	1.00	1.00	1.00	1.00
kT_{init} (keV)	0.08	0.08	0.002	0.002
kT (keV)	$1.08^{+0.05}_{-0.06}$	$1.05^{+0.06}_{-0.09}$	$0.99^{+0.34}_{-0.02}$	$1.10^{+0.06}_{-0.14}$
Mg	$0.76^{+0.51}_{-0.48}$	$1.07^{+0.39}_{-0.38}$	$3.00^{+0.71}_{-0.79}$	$1.96^{+0.50}_{-0.54}$
Si	$2.77^{+0.23}_{-0.25}$	$2.95^{+0.27}_{-0.34}$	$5.58^{+0.11}_{-0.09}$	$3.84^{+0.58}_{-0.29}$
P	$2.01^{+1.29}_{-1.25}$	$1.33^{+1.42}_{-1.33}$	$2.03^{+3.83}_{-1.86}$	$0.96^{+1.70}_{-0.96}$
S	$3.36^{+0.41}_{-0.31}$	$3.52^{+0.34}_{-0.40}$	$6.25^{+0.07}_{-0.07}$	$4.26^{+0.54}_{-0.62}$
Cl	$3.25^{+1.05}_{-1.03}$	$3.84^{+1.15}_{-1.14}$	$5.30^{+2.20}_{-2.33}$	$3.67^{+1.29}_{-1.27}$
Ar	$3.15^{+0.37}_{-0.31}$	$3.25^{+0.37}_{-0.37}$	$5.43^{+0.14}_{-0.13}$	$3.78^{+0.58}_{-0.29}$
K	$3.54^{+1.21}_{-1.20}$	$3.75^{+1.24}_{-1.22}$	$8.75^{+2.93}_{-2.88}$	$4.30^{+1.48}_{-1.44}$
Ca	$3.99^{+0.46}_{-0.37}$	$3.95^{+0.41}_{-0.44}$	$6.51^{+0.18}_{-0.18}$	$4.60^{+0.26}_{-0.13}$
Ti	$1.02^{+2.87}_{-1.02}$	$0.88^{+2.84}_{-0.88}$	$0.46^{+4.65}_{-0.46}$	$0.64^{+2.52}_{-0.64}$
Cr	$3.07^{+0.90}_{-0.88}$	$3.19^{+0.85}_{-0.83}$	$4.96^{+1.27}_{-1.29}$	$3.47^{+0.94}_{-0.94}$
Mn	$0.74^{+1.67}_{-0.74}$	$0.54^{+1.39}_{-0.54}$	$2.50^{+2.89}_{-2.50}$	$1.34^{+2.12}_{-1.34}$
Fe	$3.90^{+0.28}_{-0.29}$	$3.85^{+0.36}_{-0.28}$	$5.21^{+0.06}_{-0.06}$	$3.80^{+0.49}_{-0.37}$
Ni	$3.67^{+0.82}_{-0.85}$	$1.04^{+0.77}_{-0.74}$	$1.50^{+0.78}_{-0.79}$	$0.53^{+0.59}_{-0.53}$
Redshift (z) ($\times 10^{-3}$)	$7.80^{+0.20}_{-0.36}$	$7.59^{+0.47}_{-0.46}$	$11.04^{+3.01}_{-0.08}$	$8.90^{+0.28}_{-0.69}$
σ_v (km s^{-1})	2075^{+78}_{-77}	2067^{+88}_{-88}	1050^{+55}_{-115}	2025^{+70}_{-169}
AtomDB norm ($\times 10^{-2}$ cm^{-5})	$5.72^{+0.90}_{-0.76}$	$4.87^{+0.91}_{-0.57}$	$1.91^{+0.04}_{-0.07}$	$3.89^{+0.75}_{-0.57}$
SPEX norm ($\times 10^{63}$ m^{-3})			$2.64^{+0.06}_{-0.10}$	$5.38^{+1.04}_{-0.79}$
bvvpshock				
n_{et} ($\times 10^{11}$ cm^{-3} s)	$1.17^{+0.01}_{-0.03}$	$1.07^{+0.02}_{-0.03}$	$1.05^{+0.01}_{-0.01}$	$1.10^{+0.01}_{-0.02}$
kT (keV)	$3.87^{+0.07}_{-0.10}$	$3.77^{+0.11}_{-0.12}$	$3.62^{+0.01}_{-0.02}$	$3.73^{+0.19}_{-0.10}$
Redshift (z) ($\times 10^{-3}$)	$6.38^{+0.22}_{-0.20}$	$6.47^{+0.21}_{-0.20}$	$5.36^{+0.90}_{-1.21}$	$5.86^{+0.06}_{-0.08}$
σ_v (km s^{-1})	1868^{+39}_{-39}	1856^{+39}_{-35}	1830^{+24}_{-25}	1854^{+53}_{-26}
AtomDB norm ($\times 10^{-2}$ cm^{-5})	$3.25^{+0.14}_{-0.29}$	$3.31^{+0.31}_{-0.22}$	$2.32^{+0.10}_{-0.21}$	$2.94^{+0.17}_{-0.32}$
SPEX norm ($\times 10^{63}$ m^{-3})	–	–	$3.21^{+0.02}_{-0.02}$	$4.06^{+0.24}_{-0.44}$
Power law				
Index	3.40	3.40	3.40	3.40
AtomDB norm ($\times 10^{-2}$) (photons cm^{-2} s^{-1} at 1.0 keV)	$6.89^{+0.76}_{-0.59}$	$7.09^{+0.65}_{-0.88}$	$9.98^{+0.50}_{-0.65}$	$8.03^{+0.94}_{-0.65}$
SPEX norm ($\times 10^{44}$) (photons s^{-1} keV^{-1} at 1.0 keV)	–	–	$1.38^{+0.07}_{-0.09}$	$1.11^{+0.13}_{-0.09}$
Gaussian				
E (keV)	$3.19^{+0.01}_{-0.01}$	–	$3.19^{+0.01}_{-0.01}$	–
AtomDB norm ($\times 10^{-5}$ photons cm^{-2} s^{-1})	$1.34^{+0.54}_{-0.53}$	–	$1.69^{+0.54}_{-0.54}$	–
SPEX norm ($\times 10^{40}$ photons s^{-1})	–	–	$2.34^{+0.75}_{-0.75}$	–
Fit statistics				
C-statistic	4001.9	4004.9	4041.5	4049.2
Degrees of freedom	3423	3425	3533	3535

broadening, and normalization for the bvvrnei component. The normalization difference can be easily seen in the left and rights panels of figure 12 as the blue curve (representing the bvvrnei component) is significantly lower (∼50%) in the fit with SPEX 3.08.00. The normalization of the power-law component is ∼22% higher for the fit with SPEX 3.08.00. Therefore, the fit with SPEX 3.08.00 modeled more of the emission with the power-law component than the bvvrnei component. The broadening with SPEX 3.08.00 is approximately half of the value with 3.08.01* for the low-temperature bvvrnei component and the redshift is ∼25% higher with SPEX 3.08.00. This 25% difference is highly significant given the relatively small uncertainties. As noted earlier, the uncertainties on the redshift parameter in SPEX can be small and asymmetric.Instrumentation 2024: Ultraviolet to Gamma The agreement for the parameters of the bvvpshock component is better compared to those observed for the bvvrnei component, as all parameters agree to within 2.0σ between

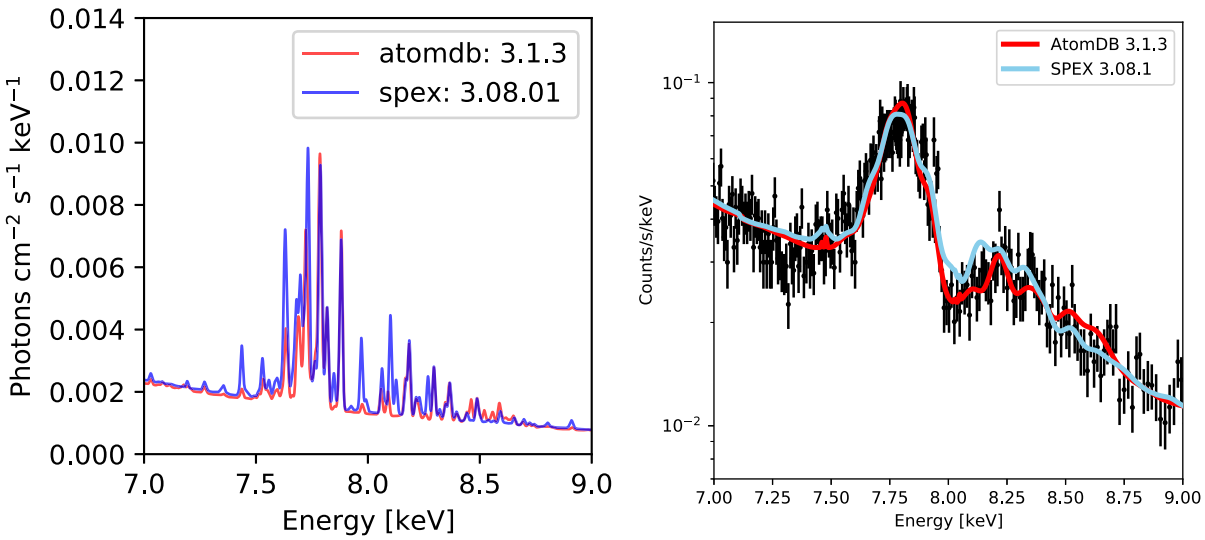

Fig. 13. Left: Model spectra from AtomDB 3.1.3 and SPEX 3.08.01* in the 7.0–9.0 keV range with parameters appropriate for the SE super-pixel "e" spectrum from table 2. Right: Data and model from the SE super-pixel "e" fit with AtomDB 3.1.3 and SPEX 3.08.01* in the 7.0–9.0 keV range.

SPEX 3.08.00 and 3.08.01*. It appears again that the redshift and the broadening are combining in different ways to produce the observed broadening of the lines. The bvvrnei component has a smaller broadening but a larger redshift for the fit with SPEX 3.08.00 compared to the fit with SPEX 3.08.01*. The larger difference between the redshifts for the bvvrnei and bvvpshock components in the fit with SPEX 3.08.00 has the effect of broadening the lines—hence the smaller value of the broadening parameter. It is interesting that the fit with SPEX 3.08.00 found such a different set of best-fitting parameters than the fit with SPEX 3.08.01*. However, the parameter space for the fit statistic is complicated with multiple local minima and it is possible that a more advanced algorithm would find a different best fit that would result in better agreement between these two versions of SPEX. Overall, the differences between the fitted parameters for the NW spectrum with SPEX 3.08.00 and 3.08.01* are larger than for the SE spectrum.

The differences in the best-fitting parameters between AtomDB 3.1.0 and SPEX 3.08.01* are smaller for the NW spectrum than for the SE spectrum. All of the fitted parameters agree at the 1.0σ level including the normalizations for the bvvrnei, bvvpshock, and power-law components and the Ni abundance, except for the Si and Ca abundances and the redshift for the bvvpshock component. There is excellent agreement for the temperatures and the ionization timescales for the thermal components. The Si and Ca abundances do agree at the 2.0σ level, so taken together with the 1.0σ agreement for the other elements, this represents remarkably good agreement between AtomDB 3.1.0 and SPEX 3.08.01*. The Ni abundances have relatively large uncertainties such that even though the best-fitting values differ by a factor of 2, they still agree within 1.0σ. The largest difference is in the redshifts for the bvvpshock components that disagree at the 2.0σ level but agree at the 3.0σ level. This is somewhat surprising as it should produce a noticeable shift in the line energies, but given the degeneracy between the redshifts and broadenings of the two thermal components, the combined effect may not be large. Even though the normalizations agree at 1.0σ, the differences are notable. The bvvrnei and bvvpshock normalizations are 25% and 13% higher, respectively, with AtomDB than with SPEX, and the power-law normalization is 12% lower with AtomDB than with SPEX. The AtomDB fit puts more of the emission in the thermal components and the SPEX fit puts more of the emission in the power-law component. This has the effect of the abundances being systematically higher in the SPEX fits, but the Fe abundances are nearly identical and the Ni abundance is higher in the AtomDB fit. Overall, the agreement between AtomDB 3.1.0 and SPEX 3.08.01* for the NW spectrum is excellent.

4.2 Ni abundance

The abundance of Ni (^{58}Ni) is of great interest in the study of SNe and SNRs because the amount of Ni synthesized can be a probe of the environment at the center of the SN explosion (Fröhlich et al. 2006; Jerkstrand et al. 2015; Fujimoto & Nagakura 2019). As noted earlier, the Ni abundance derived from the fits with AtomDB 3.0.9 and 3.1.0 changed significantly while the Fe abundance changed by a relatively smaller amount. It decreased from $30.73^{+1.85}_{-2.36}$ to $11.65^{+1.34}_{-1.26}$ in the SE spectral fit and from $3.67^{+0.82}_{-0.85}$ to $1.04^{+0.77}_{-0.74}$ in the NW spectral fit. This change is largely due to the corrections made to Kβ line emission, as described in section 4. The Fe Kβ lines of the Li-like stage (which overlap Ni Kα) had been effectively turned off by an error, and so Ni emission was trying to fill that hole in AtomDB 3.0.9. With this corrected in AtomDB 3.1.0, less Ni emission is required to compensate for this, lowering the Ni abundance. Other changes (more dielectronic recombination satellites, for example) had a similar but much lesser effect on these data as we are using an ionizing plasma model. The difference is smaller for the results with SPEX 3.08.00 and 3.08.01*. The Ni abundance decreased from $9.70^{+0.93}_{-0.80}$ to $6.62^{+0.90}_{-0.89}$ in the SE spectral fit and from $1.50^{+0.78}_{-0.79}$ to $0.53^{+0.59}_{-0.53}$ in the NW spectral fit. This is likely due to the fact that the inner shell lines and the associated excitation, dielectronic recombination, and inner shell ionization rates for low- to mid-charge Ni ions have been added to SPEX 3.08.01*. The

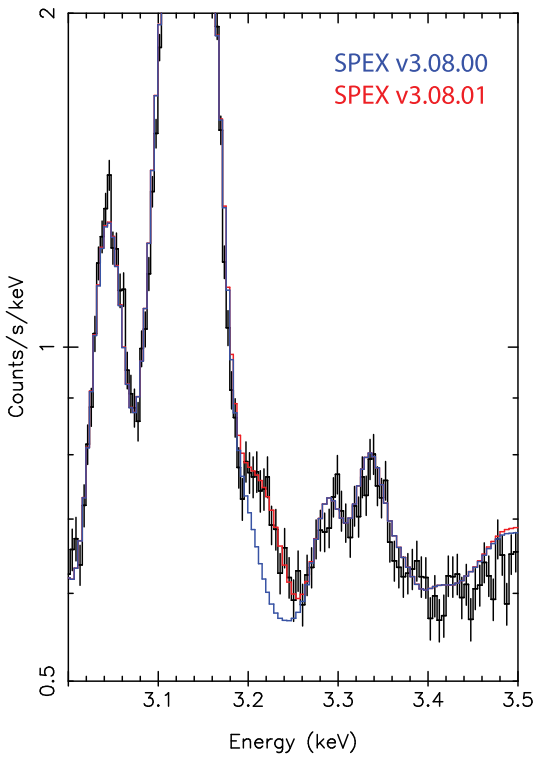

Fig. 14. Comparison of SPEX versions 3.08.00 and 3.08.01* around 3.2 keV reveals a clear difference: SPEX 3.08.01* calculates the S XV Rydberg series up to $n = 52$, significantly extending beyond the $n = 16$ limit in SPEX 3.08.00. SPEX 3.08.01* provides a better match to the observational data in this energy range.

inclusion of new lines naturally leads to a lower abundance. Figure 13 shows the differences between AtomDB 3.1.0 and SPEX 3.08.01* in the energy range containing the Ni XXVII Heα complex at ∼7.8 keV (with a significant contribution from Fe XXV Heβ at ∼7.9 keV) and the Fe XXVI Lyβ lines at ∼8.25 keV for a model spectrum with the parameters of the SE super-pixel "e" in the left panel and those models folded through the Resolve response and compared to the data in the right panel. The agreement is quite good for the Ni XXVII Heα complex and the Fe XXVI Lyβ lines but there are differences at the energies between these main complexes, presumably due to the current uncertainties in the strengths of the inner shell and dielectronic recombination satellite lines of Fe XXII, Fe XXIII, and Fe XXIV. This issue requires further investigation and may be addressed in future releases of AtomDB and SPEX to resolve this apparent discrepancy. If the abundance of Ni is important for an investigation, it is recommended to use the latest versions of AtomDB and SPEX, and to note the current level of agreement between the models.

4.3 The 3.2 keV feature

In the initial fits to the Cas A spectra with AtomDB 3.0.9 and SPEX 3.08.00, there was a clear excess of emission around an energy of ∼3.2 keV that could not be explained by the models. If this excess were real, it could potentially be radiative recombination continuum or a sign of charge exchange. However, as shown in figure 14, the excess disappears when using the updated atomic database in SPEX 3.08.01*. The excess also disappears when AtomDB 3.1.0 is used. This suggests that the excess observed with AtomDB 3.0.9 and SPEX 3.08.00 is likely due to a collection of Rydberg series of S XV with $n > 16$ that have been newly included in AtomDB 3.1.0 and SPEX 3.08.01*. These updated databases are important to support searches for relatively weak line emission from the odd-Z and trace elements such as P, Cl, and K.

4.4 Element abundances

The XRISM Resolve spectra represent the highest-resolution, most-sensitive spectra acquired to date in the 3.0–9.0 keV bandpass, which contains emission from Ar, K, Ca, Sc, Ti, V, Cr, Mn, Fe, Co, and Ni. Therefore, the Resolve spectra provide useful constraints on the abundances of these elements that can be compared with nucleosynthesis models. The amounts of these elements that are produced in the star and the subsequent explosion depend on many factors, among them the mass and metallicity of the progenitor, the mass cut between the ejecta envelope and the proto-neutron star, the delay time between core collapse and explosion, and the explosion mechanism itself (Thielemann et al. 1996; Sukhbold et al. 2016). There is compelling evidence that the SN explosion that produced the remnant we observe was asymmetric; see Orlando et al. (2021) and references therein, and Suzuki et al. (2025), Bamba et al. (2025), and Vink et al. (2025) in this special issue. The production of the odd-Z elements may be enhanced in explosive nucleosynthesis depending on the details of the explosion. Given the asymmetric nature of the Cas A explosion, spatial variations in the ratios of the even-Z and odd-Z elements might provide insights into the different nucleosynthesis processes and the stages at which they occur.

The two regions in Cas A examined in this paper provide a case study of the abundance ratios that may be used to inform nucleosynthesis models. The ratio of the elements Ar, K, Ca, Ti, Cr, Mn, and Ni with respect to Fe are listed in table 4 for the SE and NW spectra determined from the fits with AtomDB 3.1.0 and SPEX 3.08.01*. All abundance ratios agree to within 1.0σ between AtomDB 3.1.0 and SPEX 3.08.01* except for the Ni/Fe ratio for the SE spectrum, which agrees to within 2.0σ. Ti and Mn are detected in the SE spectrum as previously reported by CCD observations (Sato et al. 2021, 2023) but their abundances are consistent with zero at the 1.0σ level in the NW spectrum. Ni is detected in both the SE and NW spectra; however, its abundance is consistent with zero at the 2.0σ level in the NW spectrum. The abundance patterns are clearly different between the SE and NW spectra as the Ti/Fe, Mn/Fe, and Ni/Fe ratios are significantly lower in the NW spectrum while the Ar/Fe, Ca/Fe, and Cr/Fe ratios are comparable or perhaps slightly higher. These different abundance patterns may suggest that the innermost physical parameters (i.e., electron fraction and entropy) were inhomogeneous at the time of the explosion (Wanajo et al. 2018; Wang & Burrows 2023), consistent with the other evidence for an asymmetric explosion. A detailed analysis of these abundance ratios and the implications for nucleosynthesis models will be presented in future papers (Sato et al. 2025, XRISM Collaboration 2025).

4.5 Semi-empirical models for calibration

Cas A has been used extensively by the current generation of X-ray instruments that use CCDs on Chandra, XMM, Suzaku, and Swift as a calibration source given its line-rich spectrum and high flux. These CCD instruments are not as sensitive to small energy shifts (a few eV) as Resolve, and are almost

Table 4. Element abundance ratios with respect to Fe with AtomDB and SPEX.

	SE spectru		NW spectrum	
Abundance ratio	AtomDB 3.1.0	SPEX 3.08.01*	AtomDB 3.1.0	SPEX 3.08.01*
Ar/Fe	$0.65^{+0.06}_{-0.10}$	$0.74^{+0.09}_{-0.04}$	$0.84^{+0.11}_{-0.12}$	$1.00^{+0.18}_{-0.15}$
K/Fe	$0.86^{+0.13}_{-0.17}$	$1.04^{+0.15}_{-0.15}$	$0.97^{+0.33}_{-0.33}$	$1.13^{+0.41}_{-0.40}$
Ca/Fe	$0.72^{+0.07}_{-0.11}$	$0.84^{+0.02}_{-0.05}$	$1.03^{+0.13}_{-0.15}$	$1.21^{+0.14}_{-0.16}$
Ti/Fe	$0.90^{+0.28}_{-0.29}$	$0.88^{+0.33}_{-0.30}$	$0.23^{+0.74}_{-0.23}$	$0.17^{+0.66}_{-0.17}$
Cr/Fe	$0.50^{+0.08}_{-0.10}$	$0.63^{+0.10}_{-0.10}$	$0.83^{+0.23}_{-0.23}$	$0.91^{+0.26}_{-0.27}$
Mn/Fe	$0.50^{+0.13}_{-0.14}$	$0.73^{+0.19}_{-0.19}$	$0.14^{+0.36}_{-0.14}$	$0.35^{+0.56}_{-0.35}$
Ni/Fe	$1.06^{+0.14}_{-0.19}$	$0.64^{+0.09}_{-0.09}$	$0.27^{+0.20}_{-0.19}$	$0.14^{+0.16}_{-0.14}$

entirely insensitive to broadening and asymmetry in the line shapes. Willingale et al. (2002) used the MOS instrument on XMM to measure the distribution of redshifts throughout the remnant and Lazendic et al. (2006) used the high-resolution spectra from the High Energy Transmission Grating (HETG) on Chandra to measure the redshifts of several bright knots. The companion papers in this special issue (Bamba et al. 2025; Suzuki et al. 2025; Vink et al. 2025) expand upon this analysis by measuring not only the redshifts/blueshifts but also the widths and line shapes with the precision afforded by Resolve. Willingale et al. (2002) report a statistical error of ∼3% on the centroid of the Fe xxv Heα triplet based on XMM MOS data, compared to the 0.3% that Resolve achieved during these Cas A observations. They note a dispersion of 24.2 eV on the Fe xxv Heα centroid for the regions they analyzed, which corresponds to a velocity of 1115 km s^{-1}. The primary cause of this dispersion is the fact that the centroid of the Fe xxv Heα triplet varies as a function of temperature and ionization time-scale, which the CCD instruments are not able to constrain well. In addition, they assumed zero width for the lines in their spectral fits. Bamba et al. (2025) report absolute values of the redshifts for the Fe xxv Heα triplet from 1400 to 2160 km s^{-1} with an uncertainty of a few hundred km s^{-1} based on the Resolve data. They find that the broadening varies from 500 to 3000 km s^{-1} with the largest values occurring in the center of the remnant. Lazendic et al. (2006) report absolute values of the redshift of the Si xiii Heα triplet of 17 bright knots in Cas A ranging from 380 to 4100 km s^{-1} with uncertainties of 2.5% to 24%, corresponding to velocities of 70 to 650 km s^{-1} based on Chandra HETG data, and they assume a fixed width for the lines in their spectral fits. Suzuki et al. (2025) report absolute values of the redshift of the Si xiii Heα triplet from the Resolve SE and NW pointings ranging from 480 to 1200 km s^{-1} with uncertainties of 4.0% to 10%, corresponding to velocities of 50–130 km s^{-1}. They find that the broadening varies from 1240 to 1930 km s^{-1} with a typical uncertainty of 4% or ∼60 km s^{-1}. The inclusion of broadening is essential in order to achieve acceptable fits with the Resolve data, while the CCD data are insensitive to the broadening. Improving the fidelity of spectral models for sources such as Cas A has been a key objective of the International Astronomical Consortium for High Energy Calibration (IACHEC),[2] such as the standard model for the SNR 1E 0102.2-7219 (Plucinsky et al. 2017). The Resolve data promise to significantly improve the fidelity of the calibration models by determining the redshifts/blueshifts (energy shifts) to high precision and broadenings as a function of energy and position within Cas A.

The models using AtomDB 3.1.0 and SPEX 3.08.01* presented in tables 2 and 3 include energy shifts as redshifts and blueshifts, and broadening of the lines in the two thermal components. In addition, the bvvpshock model can produce asymmetric line profiles depending on the parameters. This effect is noticeable for the Fe K complex as noted earlier. This information is crucial if one uses the spectra from Cas A to calibrate the gain and/or spectral redistribution function of CCD instruments. An important result described in Suzuki et al. (2025) is that the redshift/blueshift for the Heα complexes is different from the Lyα lines of Si and S. Typically, when fitting CCD-resolution spectra, the same redshift/blueshift was assumed for the Heα and Lyα lines of the same element. Because the Heα triplet usually has more counts than the Lyα lines, the fit would be driven by providing the best fit to the the Heα triplet while sacrificing the fit for the Lyα line. This is further complicated by the fact that the CCD instruments cannot separate the forbidden, intercombination, and resonance lines of the triplets and the centroid of the triplet depends on the temperature and ionization time-scale. This introduces a model dependence into the determination of the centroid of the triplets that is degenerate with the redshift/blueshift. Similarly, the spatial variation of the redshifts and blueshifts as described in Bamba et al. (2025) and Vink et al. (2025) needs to be included in a calibration model if spectra from different regions are to be analyzed. In addition, Vink et al. (2025) demonstrate that the shapes of the Lyα and Heβ lines of Si and S are clearly non-Gaussian and vary with position in Cas A. Typically when fitting CCD-resolution spectra, these lines were assumed to have simple Gaussian or Lorentzian shapes, introducing another source of systematic error. For all of these reasons, an accurate determination of the line centroids and widths from a high spectral resolution instrument such as Resolve is beneficial for the development of standard models for calibration.

The models presented in this paper should be an improvement over the existing models used to calibrate CCD instruments; however, there are limitations that affect how they should be used. These models are "semi-empirical" in that they use the astrophysical plasma emission models in AtomDB and SPEX, a power-law model, and a detector background model as part of the NXB model. The two plasma models, bvvrnei and bvvpshock, were selected because they adequately represent the data in the broad band, but caution should be applied in the physical interpretation of the parameters. The plasmas along a given line of sight through Cas A undoubtedly have a distribution of conditions (temperature, ionization time-scale, abundances, etc.) that we are representing with the combination of two models, each with its own

[2] ⟨https://iachec.org⟩.

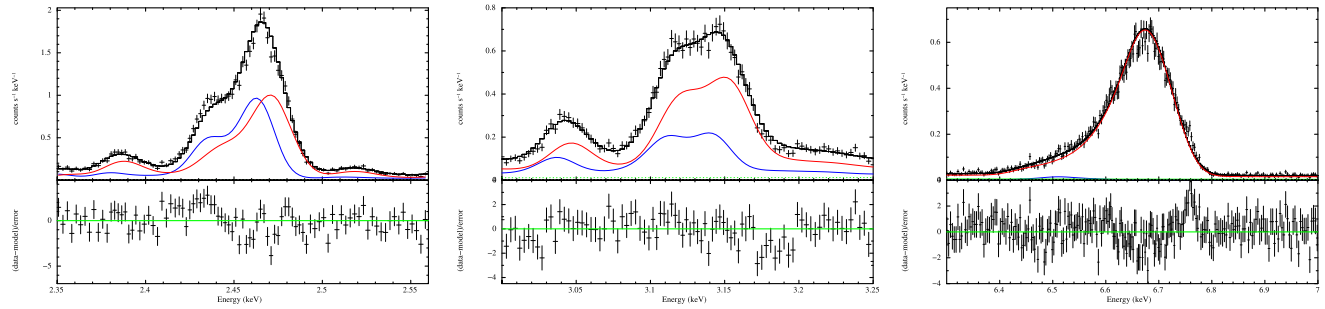

Fig. 15. Resolve spectra from the on-axis point, so-called super-pixel "e," for the SE pointing fit with XSPEC and AtomDB 3.1.0 in the S XV Heα energy range (left), the Ar XVII Heα energy range (center), and the Fe XXV Heα energy range (right). The data and total model are plotted in black, the low-temperature bvvrnei component in blue, and the high-temperature bvvpshock component in red.

limited set of parameters.In addition, these plasma emission models will change if the underlying data in the AtomDB and SPEX databases change. A standard IACHEC model typically freezes the version of AtomDB and SPEX to be used with it to eliminate this issue. Finally, the relatively large PSF of the XRISM mirrors will mix emission from multiple regions as described in sub-subsection 3.1.2, complicating the comparison with instruments that have smaller PSFs such as Chandra and XMM. The broad-band spectra are well fitted by these models, but there are issues around some of the line complexes that produce significant residuals in the fits. Figure 15 presents a close-up view of the data and model for the S XV, Ar XVII, and Fe XXV Heα triplets. Note that the two thermal components contribute roughly equally to the S XV Heα triplet, the high-temperature component provides the majority of the Ar XVII Heα triplet, and it provides essentially all of the Fe XXV Heα triplet. The combination of the two models, each with its own redshift/blueshift and broadening, has several degrees of freedom to produce a complex line shape to match the data. The two-component thermal model accurately reproduces the centroids of the line complexes but is not able to capture the complex shape of the S XV and Fe XXV Heα triplets, but it does reasonably well for Ar XVII. Therefore, these models should be sufficient for the calibration of the gain and spectral redistribution function of CCD-resolution instruments, as long as the highest fidelity is not needed for the spectral redistribution function. An alternative approach is to fit in a narrower energy range and focus on just a few lines of interest as was done by Suzuki et al. (2025), Bamba et al. (2025), and Vink et al. (2025).

5 Conclusion

We have presented an overview of two observations of the Cas A SNR conducted during the PV phase of the XRISM. One observation was centered at the bright region in the SE and the other in the NW. We presented images in the 1.5–10.0 keV band from the Xtend and Resolve instruments that identify the regions of the remnant covered by the Resolve instrument. We quantified the XRISM SSM effect by generating maps in detector pixels of the percentage of events that originate from the corresponding sky pixel region (so-called purity maps) and by generating two-dimensional matrices of the contribution of each pixel to every other pixel in the array. These calculations include the PSF effects and the attitude drifts during the observations. We find that the highest purity value for a single super-pixel (2 × 2 pixels) is 48% while the lowest is 9%, highlighting the importance of the SSM effect for an extended object with a complex morphology like Cas A. We extracted spectra from a 2 × 2 pixel region on-axis from the SE and NW observations to minimize the effects of SSM and uncertainties in the off-axis response of the mirror. We developed a semi-empirical model consisting of two thermal components (bvvrnei and bvvpshock), a non-thermal component (a power law), and detector background that fits the spectra well from 1.5 to 15.0 keV. We found that it is essential to incorporate redshifts/blueshifts and broadening of the emission lines to achieve a reasonable fit given the high spectral resolution of Resolve.

We fit these spectra with the versions of AtomDB and SPEX that were available just before the launch of XRISM and the versions that are available as of the writing of this paper. We described the changes made in the post-launch versions and documented the differences in the fitted parameters comparing the pre- and post-launch versions. The most significant difference is the abundance of Ni in the AtomDB models, which can be lower by as much as a factor of 3 in the post-launch version, depending on the spectral model. The agreement of the fitted parameters between the post-launch versions of AtomDB and SPEX is excellent, with most parameters agreeing to within 1.0σ, except for the Ni abundance, the redshifts, and broadening. The most significant disagreement between AtomDB and SPEX is the abundance of Ni. The redshift and broadening parameters are assuming different values in the fits with AtomDB and SPEX such that the combination reproduces the widths of the lines. Therefore, the differences in the individual parameters (redshift and broadening) do not manifest themselves as a large difference in the model spectra. We found that the abundance ratios of Ti/Fe, Mn/Fe, and Ni/Fe are significantly lower in the NW region than in the SE region, and that the abundances of Ti and Mn are consistent with zero in the NW region. This large variation in the abundances of these elements is further evidence of an asymmetric explosion that affected the nucleosynthesis processes. Finally, we have suggested that the models presented in this paper would be useful for the calibration of CCD-resolution instruments but we have described the limitations of their use.

Funding

PP acknowledges support from National Aeronautics and Space Adminstration (NASA) XRISM grants

80NSSC18K0988 and 80NSSC23K1656, and the Smithsonian Institution and the Chandra X-ray Center through NASA contract NAS8-03060. MA and JV acknowledge financial support from NWO under grant number 184.034.002. This work was partly supported by Japan Society for the Promotion of Science (JSPS) Grants-in-Aid for Scientific Research (KAKENHI) Grant Numbers, JP23K25907 (AB). This work was supported by the JSPS Core-to-Core Program (grant number: JPJSCCA20220002) (YT, HS) and the JSPS/KAKENHI Grant Number JP20K04009 (YT).

Acknowledgments

We thank all of the scientists, engineers, and technicians who have built the XRISM satellite, operated the mission, and developed the software that we used to analyze the data in this paper.

References

Arnaud, K. A. 1996, in ASP Conf. Ser., 101, Astronomical Data Analysis Software and Systems V, ed. G. H. Jacoby & J. Barnes (San Francisco: ASP), 17
Bamba, A., et al. 2025, PASJ, 77, S144
Bryans, P., Landi, E., & Savin, D. W. 2009, ApJ, 691, 1540
Cash, W. 1979, ApJ, 228, 939
Chevalier, R. A., & Oishi, J. 2003, ApJ, 593, L23
DeLaney, T., et al. 2010, ApJ, 725, 2038
DeLaney, T., Kassim, N. E., Rudnick, L., & Perley, R. A. 2014, ApJ, 785, 7
Fesen, R. A., et al. 2006, ApJ, 645, 283
Fesen, R. A., & Milisavljevic, D. 2016, ApJ, 818, 17
Foster, A. R., Ji, L., Smith, R. K., & Brickhouse, N. S. 2012, ApJ, 756, 128
Fröhlich, C., et al. 2006, ApJ, 637, 415
Fujimoto, S., & Nagakura, H. 2019, MNRAS, 488, L114
Grefenstette, B. W., et al. 2014, Nature, 506, 339
Hahn, M., Müller, A., & Savin, D. W. 2017, ApJ, 850, 122
Hayashi, T., et al. 2024, in Proc. SPIE, 13093, Space Telescopes and Instrumentation 2024: Ultraviolet to Gamma Ray, ed. J.-W. A. den Herder et al. (Bellingham, WA: SPIE), 130931L
Helder, E. A., & Vink, J. 2008, ApJ, 686, 1094
Holt, S. S., Gotthelf, E. V., Tsunemi, H., & Negoro, H. 1994, PASJ, 46, L151
Hughes, J. P., Rakowski, C. E., Burrows, D. N., & Slane, P. O. 2000, ApJ, 528, L109
Hwang, U., et al. 2004, ApJ, 615, L117
Hwang, U., & Laming, J. M. 2012, ApJ, 746, 130
Ishisaki, Y., et al. 2022, in Proc. SPIE, 12181, Space Telescopes and Instrumentation 2022: Ultraviolet to Gamma Ray, ed. J.-W. A. den Herder et al. (Bellingham, WA: SPIE), 121811S
Jerkstrand, A., et al. 2015, ApJ, 807, 110
Kaastra, J. S., & Bleeker, J. A. M. 2016, A&A, 587, A151
Kaastra, J. S., Mewe, R., & Nieuwenhuijzen, H. 1996, in UV and X-ray Spectroscopy of Astrophysical and Laboratory Plasmas, ed. K. Yamashita & T. Watanabe (Tokyo: Universal Academy Press), 411
Krause, O., Birkmann, S. M., Usuda, T., Hattori, T., Goto, M., Rieke, G. H., & Misselt, K. A. 2008, Science, 320, 1195
Laming, J. M., & Hwang, U. 2003, ApJ, 597, 347
Laming, J. M., & Temim, T. 2020, ApJ, 904, 115
Lazendic, J. S., Dewey, D., Schulz, N. S., & Canizares, C. R. 2006, ApJ, 651, 250
Lee, J.-J., Park, S., Hughes, J. P., & Slane, P. O. 2014, ApJ, 789, 7
Lodders, K., Palme, H., & Gail, H.-P. 2009, Landolt Börnstein, 4B, 712
Markert, T. H., Canizares, C. R., Clark, G. W., & Winkler, P. F. 1983, ApJ, 268, 134
Milisavljevic, D., & Fesen, R. A. 2013, ApJ, 772, 134
Mori, K., et al. 2022, in Proc. SPIE, 12181, Space Telescopes and Instrumentation 2022: Ultraviolet to Gamma Ray, ed. J.-W. A. den Herder et al. (Bellingham, WA: SPIE), 1218122
Noda, H., et al. 2025, PASJ, 77, S10
Orlando, S., et al. 2022, A&A, 666, A2
Orlando, S., Miceli, M., Pumo, M. L., & Bocchino, F. 2016, ApJ, 822, 22
Orlando, S., Wongwathanarat, A., Janka, H.-T., Miceli, M., Ono, M., Nagataki, S., Bocchino, F., & Peres, G. 2021, A&A, 645, A66
Patnaude, D. J., Vink, J., Laming, J. M., & Fesen, R. A. 2011, ApJ, 729, L28
Plucinsky, P. P., Beardmore, A. P., Foster, A., Haberl, F., Miller, E. D., Pollock, A. M. T., & Sembay, S. 2017, A&A, 597, A35
Porter, F. S., et al. 2024, in Proc. SPIE, 13093, Space Telescopes and Instrumentation 2024: Ultraviolet to Gamma Ray, ed. J.-W. A. den Herder & et al. (Bellingham, WA: SPIE), 130931K
Reed, J. E., Hester, J. J., Fabian, A. C., & Winkler, P. F. 1995, ApJ, 440, 706
Rest, A., et al. 2011, ApJ, 732, 3
Sato, T., et al. 2021, Nature, 592, 537
Sato, T., et al. 2025, ApJ, submitted
Sato, T., Yoshida, T., Umeda, H., Hughes, J. P., Maeda, K., Nagataki, S., & Williams, B. J. 2023, ApJ, 954, 112
Sukhbold, T., Ertl, T., Woosley, S. E., Brown, J. M., & Janka, H.-T. 2016, ApJ, 821, 38
Suzuki, S., Sonoda, H., Sakai, Y., Ohshiro, Y., Yamada, S., Agarwal, M., Katsuda, S., & Yamaguchi, H. 2025, PASJ, 77, S131
Tashiro, M., et al. 2021, in Proc. SPIE, 11444, Space Telescopes and Instrumentation 2020: Ultraviolet to Gamma Ray, ed. J.-W. A. den Herder & et al. (Bellingham, WA: SPIE), 1144422
Tashiro, M., et al. 2024, in Proc. SPIE, 13093, Space Telescopes and Instrumentation 2024: Ultraviolet to Gamma Ray, ed. J.-W. A. den Herder & et al. (Bellingham, WA: SPIE), 130931G
Tashiro, M., et al. 2025, PASJ, 77, S1
Thielemann, F.-K., Nomoto, K., & Hashimoto, M.-A. 1996, ApJ, 460, 408
Thorstensen, J. R., Fesen, R. A., & van den Bergh, S. 2001, AJ, 122, 297
Tsuchioka, T., Sato, T., Yamada, S., & Uchiyama, Y. 2022, ApJ, 932, 93
Uchida, H., et al. 2025, PASJ, 77, S23
Uchiyama, Y., & Aharonian, F. A. 2008, ApJ, 677, L105
Urdampilleta, I., Kaastra, J. S., & Mehdipour, M. 2017, A&A, 601, A85
Vink, J., et al. 2025, PASJ, 77, S154
Vink, J., Agarwal, M., Slane, P., De Looze, I., Milisavljevic, D., Patnaude, D., & Temim, T. 2024, ApJ, 964, L11
Wanajo, S., Müller, B., Janka, H.-T., & Heger, A. 2018, ApJ, 852, 40
Wang, T., & Burrows, A. 2023, ApJ, 954, 114
Willingale, R., Bleeker, J. A. M., van der Heyden, K. J., Kaastra, J. S., & Vink, J. 2002, A&A, 381, 1039
XRISM Collaboration 2024, PASJ, 76, 1186
XRISM Collaboration 2025, Nature, submitted

Received: 2025 May 29; Accepted: 2025 July 30